

## DOES THE AGN UNIFIED MODEL EVOLVE WITH REDSHIFT? UTILIZING THE X-RAY BACKGROUND TO PREDICT THE MID-INFRARED EMISSION OF AGN

D. R. BALLANTYNE<sup>1</sup>, Y. SHI<sup>2</sup>, G. H. RIEKE<sup>2</sup>, J. L. DONLEY<sup>2</sup>, C. PAPOVICH<sup>2</sup> AND J. R. RIGBY<sup>2</sup>

*Accepted by the ApJ on Aug. 31, 2006*

### ABSTRACT

Deep X-ray surveys by *Chandra* and *XMM-Newton* have resolved about 80% of the 2–10 keV cosmic extragalactic X-ray background (CXRB) into point sources, the majority of which are obscured AGN. The obscuration might be connected to processes within the host galaxy, possibly the star-formation rate. Here, we use the results of CXRB synthesis calculations as input to detailed *Cloudy* simulations in order to predict the evolution of AGN properties at several mid-IR wavelengths. Computations were performed for three different evolutions of the AGN type 2/type 1 ratio between  $z = 0$  and 1: where the ratio increased as  $(1+z)^{0.9}$ , as  $(1+z)^{0.3}$  and one with no redshift evolution. Models were calculated with the inner radius of the absorbing gas and dust at 1 pc or at 10 pc. Comparing the results of the calculations to combined X-ray and *Spitzer* data of AGN shows that the predicted spectral energy distributions are a good description of average AGNs found in the deep surveys. The existing data indicates that the mid-IR emission from an average AGN is best described by models where the attenuating material is  $\sim 10$  pc from the central engine. We present the expected *Spitzer* cumulative number count distributions and the evolution of the total AGN (type 1 + type 2) luminosity function (LF) between  $z = 0$  and 1 at rest-frame  $8\mu\text{m}$  and  $30\mu\text{m}$  for the three evolutionary scenarios. The mid-IR AGN LF will be an excellent tool to measure the evolution of the covering factor of the gas and dust from  $z \sim 0$  to 1.

*Subject headings:* galaxies: active — galaxies: evolution — galaxies: formation — galaxies: Seyfert — infrared: galaxies — X-rays: galaxies

### 1. INTRODUCTION

The earliest optical investigations of active galactic nuclei (AGN) identified two major classes of sources: type 1 AGN exhibited both broad (FWHM  $\sim 10^4$  km s<sup>-1</sup>) permitted lines and narrow (FWHM  $\lesssim 10^3$  km s<sup>-1</sup>) forbidden lines in their spectra, while type 2 AGN presented only the narrow lines (Khachikian & Weedman 1974). Unification models of AGN propose that this difference can be simply explained by an obscuring medium that surrounds a basic black hole/accretion disk system, and that different lines-of-sight into and through this obscuration give rise to the variety of observational properties witnessed in AGN phenomenology (e.g., Antonucci 1993). The obscuring medium is often visualized as a geometrically thick torus comprised of dust and molecular gas and of order a parsec in size, situated between the broad-line and narrow-line regions (e.g., Pier & Krolik 1992). Additional obscuration is likely to occur in larger structures associated with the host galaxy (e.g., Maiolino & Rieke 1995). The net unobscured view from the AGN must encompass only about 20% of the sky to explain the roughly 4:1 ratio of obscured type 2 to unobscured type 1 AGN in the local Universe (e.g., Maiolino & Rieke 1995; Ho et al. 1997). This picture is probably consistent with the recent finding from Sloan data by Hao et al. (2005) that the type 2/type 1 ratio is close to unity, because about half of the AGN appear to be well hidden in their host galaxies and would not be seen by Sloan but can only be detected with very deep spectra such as those used by Maiolino & Rieke (1995) and Ho et al. (1997). The unification model explains a number of observations. For example, the near infrared (IR) emission of many AGN shows a break near  $1\mu\text{m}$  (e.g., Rieke 1978; Neugebauer et al. 1979;

Barvainis 1987; Sanders et al. 1989), signifying dust that is at or near its sublimation temperature and hence close to the AGN. Recent *Chandra* and *XMM-Newton* X-ray observations have found that narrow Fe K $\alpha$  lines are common in both type 1 and type 2 objects, which implies the presence of cold, low-velocity gas intercepting a significant fraction of the nuclear emission (Yaqoob & Padmanabhan 2004; Nandra 2006).

While the existence of the absorbing gas around AGN is well established, the geometry, distribution, origin, and evolution of the material is largely unknown. Observations of the soft X-ray absorption can measure the equivalent neutral column density of the absorbing gas along the line of sight,  $N_{\text{H}}$ . There is a good correspondence (at the  $\sim 80\%$  level; Tozzi et al. 2006) between the sources with  $N_{\text{H}} \geq 10^{22}$  cm<sup>-2</sup> and those optically identified as being of type 2. This correspondence implies that, on average, the X-ray absorbing gas does lie outside the broad-line region. However, observations of  $N_{\text{H}}$  variability on week- to year-long timescales (Risaliti et al. 2002, 2005) argue against a simple geometry. Further evidence for a complicated geometry is found in the mid-IR. The IR spectra of most AGNs (in  $\nu f_{\nu}$  units) peak between 3 and  $10\mu\text{m}$ , and roll over at  $\sim 100\mu\text{m}$  (Andreani et al. 2003; Kuraszkiewicz et al. 2003). This behavior can be described by thermal emission by dust ranging in temperature from  $\sim 40$  K to the sublimation temperature of 1000–2000 K. Part of the cooler emission may be heated by star formation rather than the AGN (e.g., Maiolino & Rieke 1995; Schweitzer et al. 2006). Interestingly, the spectral energy distributions of type 1 and type 2 AGN are similar in the mid-IR ( $\lambda > 5\mu\text{m}$ ) (Spinoglio & Malkan 1989; Fadda et al. 1998; Kuraszkiewicz et al. 2003; Alonso-Herrero et al. 2003; Lutz et al. 2004; Rigby et al. 2004), in conflict with the predictions of many compact torus models (Pier & Krolik 1992; Granato & Danese 1994; Efstathiou & Rowan-Robinson 1995; Granato et al. 1997). All of these observations argue for a more distributed or complex geometry to the absorbing

<sup>1</sup> Department of Physics, University of Arizona, 1118 East 4th Street, Tucson, AZ 85721; drb@physics.arizona.edu

<sup>2</sup> Steward Observatory, University of Arizona, 933 N. Cherry Avenue, Tucson, AZ 85721

material around the AGN (Kuraszkiewicz et al. 2003).

If the obscuring material in AGN is distributed in a complex manner, then large object-to-object variations in properties would be expected, complicating the interpretation of both the AGN characteristics and the relationship to the host galaxy (if any). Progress can be made, however, by determining the ratio of type 2 to type 1 objects (hereafter denoted as  $R$ ) at differing AGN luminosities and redshifts. Under the unified models,  $R$  is related to the covering factor of the absorbing gas and dust, so changes in  $R$  give clues to the nature of the obscuring structures. For instance, the simplest unified model, that of an unevolving torus, predicts no evolution of  $R$ . However, over the last few years, surveys at multiple wavelengths have noted that the fraction of type 1 objects increases with AGN luminosity (Ueda et al. 2003; Barger et al. 2005; Simpson 2005; Hao et al. 2005). This trend may simply be a selection effect (Treister et al. 2004), because it is easier to find type 1 high luminosity AGN (i.e., quasars) with their broad optical lines than type 2 objects, which many models predict to be deeply buried (e.g., Hopkins et al. 2005). Moreover, at high redshifts dilution from galaxy light can overwhelm the narrow and relatively weak lines of a type 2 AGN, increasing the difficulty of identification (Moran et al. 2002). Alternatively, the luminosity dependence of  $R$  may be real, and imply that some part of the obscuring material is close enough to the central engine to be affected by high luminosities, perhaps through dust sublimation (Lawrence 1991) or radiative acceleration of magnetocentrifugal winds (Königl & Kartje 1994).

There are also hints that  $R$  increases with redshift at moderate AGN luminosities. Both Barger et al. (2005) and La Franca et al. (2005), in their analyses of deep X-ray surveys, found indications for an increase in the type 2 fraction from  $z = 0$  to  $z \sim 1$ . The sources discovered in these observations account for a large fraction of the cosmic X-ray background (CXRB) in the 2–10 keV range (Mushotzky et al. 2000; Brandt & Hasinger 2005; Worsley et al. 2005), whose spectrum can be fitted only if  $R \sim 3 - 4$  (Gilli 2004).

The implication of these observations is that if the obscuring medium around an AGN evolves with redshift then it must be connected in some way to the evolution of the host galaxy. The redshift distribution of the CXRB sources peaks at  $z \sim 1$  (Tozzi et al. 2001; Barger et al. 2002, 2005), interestingly close to where the cosmic star-formation rate (SFR) density also reaches its maximum (Hopkins 2004). This coincidence in redshift distribution suggests a possible connection between the absorbing gas and dust around an AGN and the SFR within the host galaxy (already seen in the Seyfert 1 NGC 3227; Davies et al. 2006). With this motivation, Ballantyne et al. (2006) determined that a  $R$  that evolves with both luminosity and  $z$  (constrained by the type 1 fractions observed by Barger et al. 2005) can fit the observed CXRB spectrum and X-ray number counts. However, the CXRB itself provides little constraint on the evolution as both rapid, slow or zero (e.g., Treister & Urry 2005) evolution can account for the data. A measurement of the true extent of any  $R$  evolution will provide vital information for models of galaxy and black hole evolution over this redshift range. It is therefore important to search for other observational signatures that can differentiate among various evolutions of the AGN obscuring material.

The natural next step is to consider the evolution of AGN, in particular obscured AGN, in the mid-IR where the absorbed radiation will be re-emitted. With the recent launch of the *Spitzer* Space Telescope, deep sensitive surveys of

AGN in the mid-IR are now being performed, and are finding many high- $z$  ( $z \gtrsim 0.5$ ) AGN (Lacy et al. 2004; Rigby et al. 2004; Franceschini et al. 2005; Stern et al. 2005; Alonso-Herrero et al. 2006; Barmby et al. 2006; Brand et al. 2006). Therefore, this paper presents predictions for the mid-IR number counts and luminosity functions (LFs) for three different evolutions of the type 2/type 1 AGN fraction between  $z = 0$  and 1. All three evolutions are chosen to fit the CXRB, and therefore the mid-IR predictions are consistent with the current best X-ray constraints on AGN properties and evolution. In contrast to most previous work (e.g. Silva et al. 2004), the IR predictions are not based on observed spectral energy distributions (SEDs) but are computed using the photoionization code Cloudy. This method has the advantages of being able to directly relate the X-ray properties to other wavelengths and to allow interesting physical properties of the obscuring medium to be varied and possibly constrained.

We begin in the next section by reviewing the CXRB results of Ballantyne et al. (2006), in particular the three evolutions of  $R$  that will be investigated here. The following section (§ 3) describes the Cloudy models in detail, including a description of our assumptions, and how we average individual spectra together before estimating observables. Sect. 4 then checks how well these model SEDs compare against the observed AGN X-ray and mid-IR properties. Sect. 5 presents the number counts and LFs for the three AGN evolutions and compares the predictions to the available data. In Sect. 6 we attempt to take into account the effects of star formation in the model spectra and present revised predictions. Finally, we discuss our results in Sect. 7 and summarize in Sect. 8.

This paper assumes the standard first-year *WMAP*  $\Lambda$ -dominated cosmology:  $H_0 = 70 \text{ km s}^{-1} \text{ Mpc}^{-1}$ ,  $\Omega_\Lambda = 0.7$ , and  $\Omega_m = 0.3$  (Spergel et al. 2003).

## 2. REVIEW OF CXRB MODELS

When fitting the CXRB spectrum, a key parameter is the ratio of type 2 to type 1 AGN at a given 2–10 keV X-ray luminosity  $L_X$  and  $z$ , denoted  $R(L_X, z)$ . This can be directly related to the fraction of type 2 AGN,  $f_2$ , at any  $(L_X, z)$  by  $f_2 = R/(1 + R)$ . As is commonplace, we define type 2 AGN to be those that have absorbing column densities  $N_{\text{H}} \geq 10^{22} \text{ cm}^{-2}$  in the X-ray band. If the unified model is correct then  $f_2$  is approximately equal to the covering factor of the  $\geq 10^{22} \text{ cm}^{-2}$  gas around the AGN. However, the exact distribution of this material is unknown. That is, the fraction of AGN observed to have the various obscuring columns, the  $N_{\text{H}}$  distribution, is unknown except for local bright Seyfert 2s (e.g., Risaliti et al. 1999). Under the unified model, all these columns of gas exist close to the black hole, with the observed  $N_{\text{H}}$  distribution giving the relative covering fraction of each. This distribution may also be a function of  $L_X$  and  $z$ . Therefore, constructing a CXRB synthesis model reduces to producing a model for how the X-ray absorption may vary with luminosity and redshift.

Two different assumptions on the  $N_{\text{H}}$  distribution were used by Ballantyne et al. (2006) and we adopt the same distributions here. Ten values of  $N_{\text{H}}$  were considered:  $\log N_{\text{H}} = 20, 20.5, \dots, 24.0, 24.5^3$ . In the ‘simple  $N_{\text{H}}$  distribution’, any type 1 AGN has an equal probability  $p$  of being absorbed by a

<sup>3</sup> There do exist examples of completely Compton thick AGN with estimated columns of  $\log N_{\text{H}} \geq 25$  (e.g., NGC 1068; Matt et al. 1997). The X-ray emission from these sources is so reduced that they are not an important contributor to the CXRB, but they could potentially add to the mid-IR AGN number counts and luminosity functions. However, test calculations

column of  $\log N_{\text{H}} = 20$  or  $\log N_{\text{H}} = 21.5$ . Likewise, a type 2 AGN had an equal chance of being absorbed by a column of  $\log N_{\text{H}} = 22$  or  $\log N_{\text{H}} = 24.5$ :

$$N_{\text{H}} = \begin{cases} 20.0, \dots, 21.5 & p = (1 - f_2)/4.0 \\ 22.0, \dots, 24.5 & p = f_2/6.0 \end{cases} \quad (1)$$

The second assumed  $N_{\text{H}}$  distribution was the observed Risaliti et al. (1999) distribution for type 2 AGN, and the simple one for type 1. Risaliti et al. (1999) found that in a carefully selected sample of local Seyfert 2 galaxies, 75% had  $\log N_{\text{H}} \geq 23$  with half being Compton-thick ( $\log N_{\text{H}} \geq 24$ ):

$$N_{\text{H}} = \begin{cases} 20.0, \dots, 21.5 & p = (1 - f_2)/4.0 \\ 22.0, \dots, 23.5 & p = f_2/8.0 \\ 24.0, 24.5 & p = f_2/4.0 \end{cases} \quad (2)$$

Ballantyne et al. (2006) considered many different parameterizations for possible evolutions of  $R(L_X, z)$ , and presented results for two cases that could fit the observed shape of the CXRB and X-ray number counts (the results were independent of the  $N_{\text{H}}$  distribution assumed). The first evolution had an initial  $z = 0$ ,  $L_X = 10^{41.5}$  erg s<sup>-1</sup> type 2/type 1 ratio of  $R_0 = 4$ , comparable to previous optical measurements (Maiolino & Rieke 1995), and required only gradual redshift evolution:

$$f_2 = K(1 + z)^{0.3}(\log L_X)^{-4.8}, \quad (3)$$

where  $K$  is a constant defined by  $R_0$ . This evolution of the absorbing gas around AGNs also provided an acceptable fit (reduced  $\chi^2 = 1.3$ ) to the type 1 fractions measured by Barger et al. (2005) at different luminosities and redshifts. The second parameterization presented by Ballantyne et al. (2006) was inspired by the SDSS measurement of  $R_0 = 1$  (Hao et al. 2005), and required much more rapid redshift evolution in order to fit the CXRB:

$$f_2 = K(1 + z)^{0.9}(\log L_X)^{-1.3}. \quad (4)$$

This model did a poor job fitting the Barger et al. type 1 fractions (reduced  $\chi^2 = 2.6$ ). In both these cases, the  $z$  evolution was halted at  $z = 1$ , because there was no constraint on  $f_2$  at higher redshifts. Also, the increase in  $f_2$  with  $z$  may slow significantly at  $z \sim 1$  if the gas obscuring the AGN is connected to the cosmic SFR density.

The CXRB spectrum and X-ray number-counts can also be fit with a model where the type 2/type 1 AGN ratio does not evolve with redshift (e.g., Treister & Urry 2005). This scenario should be considered as a null-hypothesis in our investigation. One of the unevolving parameterizations that Ballantyne et al. (2006) presented that fits the CXRB spectrum is

$$f_2 = K \cos^2 \left( \frac{\log L_X - 41.5}{9.7} \right), \quad (5)$$

where  $R_0 = 4$ . This model does have a modest luminosity dependence, but this will not affect the comparison between the  $z$ -dependent evolutions above.

Figure 1 shows contours of  $R(L_X, z)$  for the three evolutions presented here. The different models have very different predictions for the ratio of obscured to unobscured AGN particularly at  $0.5 \leq z \leq 1$ . The rapidly evolving model (Eq. 4)

showed that the inclusion of such sources did not change our  $N_{\text{H}}$ -averaged SEDs in the mid-IR from which we make our predictions. Thus, objects with columns of  $\log N_{\text{H}} \geq 25$  can be safely excluded from our calculations. See Sect. 3.5 for details on the construction of the  $N_{\text{H}}$ -averaged SEDs.

predicts ratios of 4:1 to 5:1 for quasars at  $z \sim 1$ , as opposed to the 2:1 to 1:1 ratios predicted by the other two evolutions. At lower luminosities and redshifts, the slower evolution model (Eq. 3) predicts a larger value of  $R$  than the other possibilities. This paper will explore how these differences manifest themselves in the IR AGN number counts and LFs.

### 3. CALCULATION OF AGN SPECTRAL ENERGY DISTRIBUTIONS

#### 3.1. General Methodology

If the gas and dust causing the X-ray absorption are also responsible for the majority of the IR emission from an AGN, then it may be possible to discriminate among the three evolutions by mid-IR measurements. In this case, the IR emission for a given X-ray  $N_{\text{H}}$  can be predicted by a photoionization model, and since the evolution of  $N_{\text{H}}$  is predicted by the CXRB models, the subsequent evolution in different IR bands can be predicted. The photoionization models also allow the ability to vary parameters such as the location, density distribution and dust content of the absorbing gas, which may result in constraints to some of these physical properties.

We employ the photoionization code Cloudy v. 05.07.06 (Ferland et al. 1998) to compute the IR emission of the absorbing gas. Although the last decade has seen significant work on the exact radiative transfer problem of IR photons through a dust torus (Granato & Danese 1994; Efstathiou & Rowan-Robinson 1995; Granato et al. 1997; Dullemond & van Bemmelen 2005; Fritz et al. 2006), these techniques do not provide an easy correspondence to the X-ray absorbing gas. Furthermore, they ignore gas-grain interactions such as gas-heating by photoelectric emission and grain charging by electron capture (Weingartner & Draine 2001). These effects are included in the latest versions of Cloudy which also uses a new, more physical grain model where the size distributions of both the silicate and graphite components as well as PAHs are each resolved into 10 size bins. The dust module in Cloudy also takes into account the non-equilibrium temperature spiking process that affects the very small grains (Purcell 1976; Sellgren 1984; van Hoof et al. 2004). The computed SEDs therefore include all the detailed dust physics of the latest torus models, but also allow a connection to the X-ray properties.

The disadvantage to this technique is that it requires a simplification of the actual IR emission region which may be quite complex (e.g., Nenkova et al. 2002; Dullemond & van Bemmelen 2005). Furthermore, there are many instances of local AGN whose X-ray absorbing gas seems to be mostly dust-free (Weingartner & Murray 2002), or where only a fraction of the total column is dusty (Ballantyne et al. 2003). In addition, the radiative transfer techniques employed in Cloudy are less sophisticated than those used in the multi-dimensional torus models (Ferland 2003). However, our goal is not to reproduce the SEDs of individual objects, but to make predictions for the average properties of an ensemble of AGN at a given  $L_X$  and  $z$ . Since even in local AGN, there is a wide range of IR properties (Weedman et al. 2005; Buchanan et al. 2006), it is plausible that no systematic errors will result from the simplicity of the model calculations. This expectation is tested against real data in Sect. 4.

#### 3.2. Cloudy Model Setup and Assumptions

Each Cloudy model has a simple setup: a constant AGN spectrum with a 2–10 keV luminosity  $L_X$  strikes a cloud with

an inner radius  $r$  pc from the continuum source. The gas has abundances similar to the Orion nebula (using the ‘abundances Orion’ command in Cloudy), and has a uniform hydrogen density of  $10^4 \text{ cm}^{-3}$ , which is typical for a molecular cloud. The calculation proceeded through the cloud until the X-ray measured column density reached a value  $N_{\text{H}}$  (utilizing the ‘stop effective column density’ command<sup>4</sup>). The ionizing spectrum was defined using the ‘agn’ continuum in Cloudy with an X-ray photon-index of 1.9, a big blue bump temperature of  $1.4 \times 10^5 \text{ K}$  (appropriate for  $10^7 M_{\odot}$  black hole accreting at one-tenth of its Eddington rate), and an  $\alpha_{\text{ox}} = -1.4$ . While this is a common value of  $\alpha_{\text{ox}}$  over a wide range of luminosity and redshift, Steffen et al. (2006) showed that this parameter is anti-correlated with the UV luminosity of the AGN. There is significant scatter in this relation, however, and to date only optically selected, very high luminosity,  $z > 4$  quasars have been found to typically exhibit significantly lower values of  $\alpha_{\text{ox}}$  (e.g., Shemmer et al. 2006). Unfortunately, it is unknown if there is any relation between  $\alpha_{\text{ox}}$  and the infrared properties of AGN.

Cloudy has two stored grain (graphite and silicate) distributions. One, denoted ‘Orion’, is based on the flatter reddening observed in star-forming regions due to a lack of small grains. The other, called ‘ISM’, reproduces the standard Galactic reddening law. Since it has been argued that small dust grains close to an AGN will be preferentially destroyed (Maiolino et al. 2001; Weingartner & Murray 2002), we employ the Orion grains in our models; however, two grids with the ISM grains were also computed to check the sensitivity of the results to this assumption. PAHs were included in all calculations.

Finally, consistent with the unified model, we set the covering factor of the illuminated gas and dust equal to  $f_2$  when  $N_{\text{H}} \geq 10^{22} \text{ cm}^{-2}$  or  $1 - f_2$  otherwise. This assumption may run into trouble at high luminosities if, as has been proposed (e.g., Sanders et al. 1989), quasars evolve over time from being completely buried to unobscured. In this model, the covering factor of the obscuring gas and dust need not be related to the fraction of type 2 sources at any  $(L_X, z)$  pair. However, for the time being we will continue to assume this is the case and that the unified model is valid over all luminosities. Sect. 7.4 tests the validity of this assumption.

Since the covering factor is variable between  $z = 0$  and 1 when using the evolutions described by equations 3 and 4, Cloudy models also had to be calculated as a function of  $z$  for each  $L_X$  and  $N_{\text{H}}$ . For completeness, the cosmic microwave background with the appropriate temperature and intensity for the particular  $z$  was added to the illuminating spectrum using the ‘cmb’ command.

### 3.3. Choosing the Inner Radius of the Absorbing Gas

The minimum distance from the radiation source that a dust grain can typically survive is the sublimation radius, which is a function of both the grain size and composition as well as the luminosity of the AGN (Barvainis 1987; Laor & Draine 1993). For a bolometric AGN luminosity of  $10^{46} \text{ erg s}^{-1}$ , Laor & Draine (1993) show that sublimating grains exist from  $\sim 0.2$  pc (for the largest grains) all the way to  $\sim 4$  pc (for the smallest grains) from the central engine. Since the Cloudy models resolve the grains in both size and composition, we

are unable to pick an inner radius for the absorbing material that will self-consistently account for sublimating grains over all grain radii. For example, if we chose an inner radius of  $\sim 4$  pc so that only the smallest grains are sublimating then we are neglecting the near-IR emission from the larger grains that can exist much closer to the AGN. In contrast, if we pick a radius of  $\sim 0.2$  pc, the sublimation radius for the largest grains, then the smaller grains would be above their sublimation temperatures and radiating at inappropriately small wavelengths. Self-consistently accounting for grain destruction is a complicated procedure especially if it occurs only over a fraction of the cloud depth. Therefore, as a compromise between the two extremes, we have selected the inner radius of the absorbing cloud to be  $r = 1$  pc. For the Orion (ISM) grain distributions, sublimation temperatures for the smallest grains begin to be reached at  $\log L_X = 43.5$  (43.25) and no attempt is made to correct the results for grains radiating above their sublimation temperature. This will have the largest effect on SEDs computed at the highest luminosities ( $\log L_X \gtrsim 46$ ) at which a significant portion of the hot dust emission is shifted to shorter wavelengths than observed. These high luminosity objects are rare, and as our predictions depend on the AGN luminosity function, this issue will have only a small effect on our predictions from  $z = 0-1$ . Moreover, Sect. 4 shows that when averaged over the  $N_{\text{H}}$  distribution, the computed SEDs have very similar IR properties to the ensemble of observed AGN.

Choosing a fixed inner radius for the attenuating cloud is a different but equally valid technique as that employed by recent models of dust tori, which select the inner radius for a single grain size and change it with AGN luminosity (e.g., Fritz et al. 2006). This latter strategy may be more appropriate for fitting individual SEDs, but we are most interested in determining the properties of average AGNs that are being selected in the deep *Chandra* and *Spitzer* surveys. Thus, it is more appropriate to think of the inner radius of  $r = 1$  pc as an average distance or as a radius where there is a significant density enhancement in an average AGN.

In this context, we also calculated models with the inner radius at  $r = 10$  pc. As mentioned in § 1, there is significant observational evidence that dust emission over a range of radii is required to fit the observed SEDs of many AGN. In addition, if the obscuring material is connected to a galactic-scale phenomenon such as a starburst ring, then a significant density enhancement at distances of  $\sim 10$  pc may be common. It is therefore interesting to check if the ensemble of AGNs shows evidence for enhanced density at these distances. Clearly, dust emission from  $\sim 10$  pc may be too cool to account for some of the observed near-IR AGN properties (sublimation temperatures were reached at  $\log L_X = 45.5$  for the Orion grains), but it may be important in the mid-IR.

### 3.4. The Model Grids

Our interest is in predicting the mid-IR properties of AGN as a function of the 2–10 keV X-ray luminosity  $L_X$  and  $z$  using the fits to the CXRB as constraints. Thus, we iterate from  $\log L_X = 41.5$  to 48 (in steps of 0.25), and  $z = 0$  to 5 (in steps of 0.05) as we did in constructing the CXRB synthesis model (Ballantyne et al. 2006). For each  $(\log L_X, z)$  pair we compute using the evolution equations 3, 4 or 5 the value of  $f_2$ , and therefore the covering factor of absorbing gas around the black hole (if the unified model is correct). A Cloudy model is then computed for each  $\log N_{\text{H}} = 20.0, 20.5, \dots, 24.0, 24.5 \text{ cm}^{-2}$ . In practice, because the red-

<sup>4</sup> We confirmed that the X-ray hardness ratio derived from the Cloudy models using this method agrees with ones calculated with a `wabs*power` model in XSPEC.

shift evolution is only constrained from  $z = 0$  to 1, we assume that there is no redshift evolution in  $f_2$  when  $z > 1$  (see also § 2). Therefore, the photoionization models were calculated only up to  $z = 1$ , and the  $z = 1$  models are then used at  $z > 1$ . This resulted in 5670 individual Cloudy models for the two redshift-dependent evolutions (eqs. 3 and 4) and only 270 models for the unevolving torus model (eq. 5).

Grids were computed for all three evolutions with the inner radius of the absorbing cloud at  $r = 1$  pc and at  $r = 10$  pc. For ease of reference, we will now refer to results from individual grids using a compact label based on the initial  $R_0$  and  $r$  of the grid (e.g., 4:1/1pc, 1:1/10pc, or nozevol/1pc).

### 3.5. Constructing the Final Spectral Energy Distributions

At this point, within every grid, there are 10 Cloudy models at each  $(L_X, z)$  pair for the different  $N_H$  values. The photoionization models provide several different spectra for each computation. The ones of most interest for these purposes include the sum of the transmitted continuum and outward directed diffuse emission from the illuminated material (corresponding to observing the AGN through the cloud), and the reflected emission from the inner surface of the cloud. However, under the unified model, since all columns exist around the AGN, we would observe reflected emission from all  $N_H$  including the Compton-thick columns. Evidence for this can be found in the X-ray spectra of many Seyfert 1s where narrow Fe  $K\alpha$  lines are observed from optically-thick material out of the line-of-sight (e.g., Yaqoob & Padmanabhan 2004). Thus, to construct the SED for each  $N_H$ , a weighted average of the reflected emission from all 10  $N_H$  models is added to the transmitted+outward diffuse spectrum for that particular  $N_H$ . The weights in the average followed the chosen  $N_H$  distribution, so that for the ‘simple  $N_H$  distribution’ the reflected spectrum for all the  $N_H \geq 10^{22} \text{ cm}^{-2}$  models had a weight of  $f_2/6$  (eqn. 1). In this way, we calculate a spectrum for each  $N_H$  that corresponds to observing the AGN through that column but also takes into account the reflected emission from the other columns that lie out of the line of sight. We refer to these SEDs as the ‘unified SEDs’.

The last step before calculating specific predictions for the mid-IR wavebands is to average these unified SEDs together to find an average AGN SED at this luminosity and redshift. This is the same procedure as is used when constructing CXRB synthesis models (e.g., Gilli et al. 1999, 2001). Two different  $N_H$  distributions (described in Sect. 2) are used to generate this final SED. Figure 2 shows examples from the 4:1/1pc and 4:1/10pc grids when  $\log L_X = 43$  and  $z = 0.45$  (the spectra are plotted in the rest frame). At this luminosity and redshift, eqn. 3 gives a type 2 AGN fraction of 0.754 ( $\bar{R} \approx 3$ ), so the  $N_H$ -averaged spectrum will be dominated by the ‘unified SEDs’ with  $N_H \geq 10^{22} \text{ cm}^{-2}$ . The Risaliti et al. distribution, with half of the type 2 AGN being Compton-thick, only makes a significant difference to the average SED at wavelengths  $> 30 \mu\text{m}$ . The X-ray part of the averaged SED is only moderately absorbed as is required to fit the CXRB (see below).

An interesting property of the  $N_H$ -averaged SED shown in the top panel of Fig. 2 is the strength of the silicate emission at  $\sim 10 \mu\text{m}$  even though at large values of  $N_H$  silicate absorption is commonly observed. This emission, as well as the majority of the other emission lines, is a result of including the reflected emission from the hot inner walls of the absorbing cloud. The fact that silicate emission is predicted even for spectra which are dominated by type 2 AGN is interesting

given that the majority of AGN with typical Seyfert 2 levels of  $N_H$  show silicate absorption (Shi et al. 2006), although some exceptional cases do show emission (Sturm et al. 2006). As our main focus is on the overall continuum properties, the behavior of this feature, in addition to the emission lines, will not significantly influence the predictions. We do note, however, that the  $N_H$ -averaged SED from the  $r = 10$  pc model (lower panel in Fig. 2) exhibits significantly weaker silicate emission than in the case where the inner radius of the attenuating material lies at 1 pc.

## 4. PROPERTIES OF THE MODEL SEDS

Given the simplifying assumptions made in these calculations, it is important to verify that the  $N_H$ -averaged SEDs are fair representations of reality, particularly in the mid-IR where the predictions of the number-counts and LFs will be made. Our goal is not to fit the SEDs of individual objects, but to compare various properties of the ensemble of models to the large samples of AGN being studied in the deep, multi-wavelength surveys. This is valid because we will only be making predictions (cumulative number count distributions and luminosity functions) that will be compared against data that are averaged over many individual objects.

The photoionization models greatly ease the ability to make the comparisons to data, as we are able to calculate the observed X-ray flux (in addition to the IR fluxes) in multiple bands. In this way we can make true multiwavelength comparisons to data.

The ‘simple  $N_H$  distribution’ (eqn. 1) was used for the models presented throughout this section. Employing the Risaliti et al. (1999) distribution (eqn. 2) only makes a very minor difference to observables like colors, so these results are not presented here.

In this section and throughout the paper, model IR fluxes were computed using the predicted flux at the specific wavelength of interest (e.g.,  $3.6 \mu\text{m}$ ,  $8 \mu\text{m}$ , etc.). *Spitzer* of course measures an average flux over a passband. Comparing fluxes computed at one wavelength with those averaged over the *Spitzer* passband yielded differences of a few percent. Given the level of the systematic assumptions made in the calculations, this difference in predicted fluxes is negligible. For this reason we also do not consider the wavelength dependent efficiency of the *Spitzer* passbands.

### 4.1. Mid-IR to X-ray Flux and Luminosity Ratio

If the attenuating gas and dust around an AGN was strictly responsible for the thermal IR emission, then a correlation might be expected between the relative strength of the IR flux and the absorbing column density. That is, the most obscured sources should produce the largest mid-IR to X-ray flux ratio. However, mid-IR observations of X-ray selected AGN have shown no correlation at all between the X-ray hardness ratio (a proxy for the absorbing column  $N_H$  since more heavily absorbed objects will appear harder) and the strength of the IR flux relative to the hard X-ray (Lutz et al. 2004; Rigby et al. 2004).

In Figure 3 we test the existence of this expected correlation with the ‘unified SEDs’ computed from the Cloudy models. Panel (a) plots the  $f_{24 \mu\text{m}}/f_{2-8 \text{ keV}}$  ratio as a function of the  $f_{2-8 \text{ keV}}/f_{0.5-2 \text{ keV}}$  ratio for all the ‘unified SEDs’ with  $z < 3$  in the 4:1/1pc grid (the results are not significantly different using other evolutions). Panel (b) shows the same data except only includes the results for models with  $\log L_X < 43$ . The black region shows where models with  $\log N_H < 23$  fall,

the red area plots models with  $23 \leq \log N_{\text{H}} < 24$ , and the blue region denotes models with  $\log N_{\text{H}} \geq 24$ . The green squares are combined *Chandra* and *Spitzer* data on AGN in the *Chandra* Deep Field South (CDFs; Rigby et al. 2004).

The first important result to note is that only objects with columns  $\log N_{\text{H}} \geq 24$  produce the largest relative  $24\mu\text{m}$  fluxes. This is in agreement with the results of Rigby et al. (2004) who employed local observed SED templates to predict the  $f_{24\mu\text{m}}/f_{2-8\text{ keV}}$  ratio. Panel (b) of Fig. 3 shows that the lowest  $f_{24\mu\text{m}}/f_{2-8\text{ keV}}$  ratios are found from objects with  $\log L_X > 43$  if the inner radius of the absorber is at 1 pc. However, if  $r = 10$  pc then the absorber is less ionized for a given  $\log L_X$ , and larger hardness ratios are possible, which enable these models to fill much more of the observed parameter space (panels (c) and (d)). Interestingly, panel (d) shows that when the inner radius of the attenuating material is at 10 pc, the lowest  $f_{24\mu\text{m}}/f_{2-8\text{ keV}}$  ratios are found from objects with  $\log L_X < 43$ , the opposite of what was found when  $r = 1$  pc. This can be understood by using Fig. 2 as a guide. The  $r = 1$  pc models produce significant hot dust emission that peaks at wavelengths  $< 24\mu\text{m}$ , while the 10 pc models have much cooler dust emission peaking at  $24\mu\text{m}$  or even longer (the 2–8 keV flux is basically identical between the two cases). Therefore, as the spectra are redshifted, the hot dust emission in the  $r = 1$  pc models moves through the  $24\mu\text{m}$  band and keeps the mid-IR/X-ray ratio high. In contrast, the flux at  $24\mu\text{m}$  would be lower at the same  $L_X$  and  $z$  for the  $r = 10$  pc models since the peak mid-IR emission would be redshifted out of this band. The CDFS survey, being a pencil-beam deep field, is dominated by AGN with  $\log L_X < 44$  (Zheng et al. 2004). This would seem to indicate that the observed-frame  $24\mu\text{m}$  emission may originate, on average, from material a few pc removed from the AGN.

It is also interesting to note the few objects with enhanced  $f_{24\mu\text{m}}/f_{2-8\text{ keV}}$  ratios that are found at very soft hardness ratios. None of the computed ‘unified SEDs’ were able to account for these sources. They may have increased  $24\mu\text{m}$  flux due to star-formation heating. However, given the significant number of assumptions made in these calculations on ionizing spectrum, chemical composition, geometry, etc., it is more important that the models account for the broad properties of the ensemble.

Figure 4 plots the same quantities as Fig. 3(a) except the measurements are made from  $N_{\text{H}}$ -weighted spectra. As alluded to in the previous section the X-ray hardness ratios of these SEDs do not span a wide range. This is necessary to fit the CXRB which is well described by a  $\Gamma = 1.4$  power-law between 1 and 20 keV (Kushino et al. 2002; Lumb et al. 2002; De Luca & Molendi 2004). In Fig. 4 we denote the  $f_{2-8\text{ keV}}/f_{0.5-2\text{ keV}}$  ratio for such a power-law with the vertical dotted line. The red region denotes the  $f_{24\mu\text{m}}/f_{2-8\text{ keV}}$  ratio measured from models with  $z < 1$  and  $\log L_X < 44$ . The recent deep X-ray surveys all show that these AGN dominate the production of the 2–10 keV CXRB (Ueda et al. 2003; Barger et al. 2005; La Franca et al. 2005). Indeed, the red area is bisected by the hardness-ratio appropriate for producing the correct shape of the CXRB.

Fig. 3 shows that the model SEDs, which were constructed based on the assumptions of the unified model, can fully account for the distribution of data points from the CDFS. In fact, no correlation between  $f_{24\mu\text{m}}/f_{2-8\text{ keV}}$  and the hardness ratio is predicted by these models. This is, in part, due to the poor translation from hardness ratio to absorbing  $N_{\text{H}}$  col-

umn for surveys that span a large range in redshift. For a given  $N_{\text{H}}$ , the observed hardness ratio will decrease with increasing redshift. To correct for this problem, Rigby et al. (2006) and Lutz et al. (2004) plotted the ratio of the absorption-corrected 2–10 keV luminosity to the  $6\mu\text{m}$  luminosity versus the inferred  $N_{\text{H}}$  for AGN with known or estimated redshifts. These authors again found no correlation of the X-ray-to-mid-IR luminosity with absorbing column at  $z = 0$  or at  $z = 1$ . Figure 5 shows the predicted  $L_X/\nu L_\nu(5.7\mu\text{m})$  versus  $\log N_{\text{H}}$  plot for the unified SEDs resulting from the 4:1/1pc and 4:1/10pc grids. As the ratios are constructed using rest-frame quantities, only one redshift is plotted ( $z = 0.7$ ). The predicted ratios are color-coded based on X-ray luminosity with black triangles corresponding to  $46 < \log L_X \leq 48$ , red triangles denoting  $44 < \log L_X \leq 46$ , and blue triangles showing the results for  $41.5 \leq \log L_X \leq 44$ . The green squares and cyan stars plot the ratios observed by Rigby et al. (2006) and Lutz et al. (2004), respectively.

Both the 1 pc and 10 pc models cover roughly the same region in the  $L_X$  to  $\nu L_\nu(5.7\mu\text{m})$  ratio, but can only explain about the upper half of the observed data points. Evidently, these unified SEDs do not always produce enough 5.7–6 $\mu\text{m}$  emission to account for the observations. Star-formation is a possible culprit, but Lutz et al. (2004) correct for this by decomposing their spectra using the PAH emission as a guide to the star-formation strength. This effect may also be a result of omitting the host galaxy from the calculated SEDs, which will become more important at low AGN luminosities (we return to this point in Sect. 4.3). Lutz et al. (2004) do suggest this may be a possible source of error in their measured  $6\mu\text{m}$  fluxes, but it is unlikely to account for the roughly factor of 10 disagreement for some of the points. Perhaps the disagreement is a result of missing hot dust emission from within 1 pc. Replotting the figure with results using the ISM grain distribution that includes smaller (and hence hotter) grains results in only a very small decrease in the  $L_X$  to  $\nu L_\nu(5.7\mu\text{m})$  ratio. This result indicates that more hot dust emission may be helpful but is again unlikely to solely account for the large discrepancies implied by some of the data points. It seems more likely that the disagreement is due to a combination of all three effects, as well as possible measurement errors and the failure of one of our fundamental assumptions in the geometry of the absorber. A full investigation of this problem is beyond the scope of this paper and is left for future work.

Finally, it is interesting that in the 4:1/1pc models, the largest  $L_X$  to  $\nu L_\nu(5.7\mu\text{m})$  ratios are found at the highest  $L_X$ , but, for the 4:1/10pc models, they are found at the lowest  $L_X$ . Indeed, when  $r = 10$  pc, roughly the same spread of  $L_X/\nu L_\nu(5.7\mu\text{m})$  is found for  $\log L_X > 46$  and  $\log L_X \leq 44$ . When the absorbing material is closer to the ionizing source, it is easier to produce hot dust emission at low X-ray luminosities, so as  $L_X$  increases, there is a slower corresponding increase in  $\nu L_\nu(5.7\mu\text{m})$ . At larger distances, it is more difficult to produce hot dust and, for low  $L_X$ , increasing  $L_X$  also results in little response at  $\nu L_\nu(5.7\mu\text{m})$ . The sources plotted by Rigby et al. (2006) have  $\log L_X \lesssim 44.7$ , and are thus consistent with either value of  $r$ .

#### 4.2. Infrared Colors

Another important check on our calculation strategy is the distribution of the observed-frame IR colors. In Figs. 6 and 7 color-color diagrams are constructed from the  $N_{\text{H}}$ -weighted SEDs and compared with *Spitzer* data presented by Lacy et al. (2004). In the first case, which examines only IRAC colors,

the vast majority of the models fall within the selection region determined by Lacy et al. (2004). Fig. 7 compares a MIPS color to an IRAC one. In both cases, although there are a few data points that are significantly redder or bluer than the predicted colors, most of the  $N_{\text{H}}$ -averaged SEDs have colors that are very similar to the observed data.

The curves traced out by the models in both the color-color plots are the changes caused by the IR slope (which depends on  $L_X$ ) being redshifted through the observed bands. For example, the ‘tail’ at constant  $f_{5.7\mu\text{m}}/f_{3.6\mu\text{m}}$  in the 1:1/10pc panel of Fig. 7 is caused by AGN with  $\log L_X < 43$  over all  $z$ . At low  $L_X$  and an inner radius of 10 pc, there is little hot dust emission, so the SED does not begin to rise until  $\sim 8\mu\text{m}$  (Fig. 2). The  $5.7\mu\text{m}$ -to- $3.6\mu\text{m}$  slope is therefore nearly unchanged over the  $z$  range considered here, but  $f_{24\mu\text{m}}/f_{5.7\mu\text{m}}$  falls with redshift as less emission gets redshifted into the  $24\mu\text{m}$  band.

Another useful way of comparing predicted to observed mid-IR colors is the histogram of  $\nu f_\nu(24\mu\text{m})/\nu f_\nu(8\mu\text{m})$ . Brand et al. (2006) found that the vast majority of X-ray sources in the XBoötes survey had  $\nu f_\nu(24\mu\text{m})/\nu f_\nu(8\mu\text{m}) \approx 0$ . In Figure 8, histograms of this ratio are presented from the  $N_{\text{H}}$ -averaged SEDs for both the nozevol/1pc and nozevol/10pc grids (black lines), as well as the 1:1/1pc and 1:1/10pc grids (red lines). To more easily compare with the Brand et al. (2006) result, the histograms only included SEDs with  $f_{0.5-7\text{keV}} > 7.8 \times 10^{-15} \text{ erg cm}^{-2} \text{ s}^{-1}$ , the flux limit of the XBoötes survey, and  $f_\nu(24\mu\text{m}) > 0.3 \text{ mJy}$ . In contrast to a strong peak at  $\nu f_\nu(24\mu\text{m})/\nu f_\nu(8\mu\text{m}) \approx 0$ , the models computed with  $r = 1 \text{ pc}$  tend to have bluer mid-IR colors with the peak at  $\nu f_\nu(24\mu\text{m})/\nu f_\nu(8\mu\text{m}) \approx -0.6$ . The situation improves slightly when  $r = 10 \text{ pc}$ . In this case, the histogram is much flatter with only a slight enhancement of sources with negative values of  $\nu f_\nu(24\mu\text{m})/\nu f_\nu(8\mu\text{m})$ . These results indicate that models with the inner radius of the absorbing material  $\sim 1 \text{ pc}$  away from the AGN do not produce enough  $24\mu\text{m}$  emission to reproduce the mid-IR colors of an average AGN. This flux could be added by heating by intense star-formation, or, as indicated here, by emission from material at larger distances. The 1:1 evolution models produce fewer bluer SEDs than the unevolving AGN model. This is likely a result of the greater fraction of obscured large- $L_X$  AGN at  $z \sim 1$ .

#### 4.3. Absolute Fluxes

The final test to be performed here is comparing the absolute observed-frame fluxes predicted by the  $N_{\text{H}}$ -weighted SEDs with the available data. Figure 9 plots the predicted  $8\mu\text{m}$  and  $3.6\mu\text{m}$  fluxes against the predicted 0.5–10 keV fluxes. The black crosses are from the 4:1/1pc models, while the blue triangles plot the predictions from the 4:1/10pc models. Only models with  $z < 3$  were plotted on the Figure. To compare with these predictions, the IR and X-ray data from sources in the Extended Groth Strip (EGS) were taken from Barmby et al. (2006) and are plotted as red squares.

Fig. 9 reveals an important limitation in our  $N_{\text{H}}$ -weighted SEDs. As expected, there is a strong correlation between the IR and X-ray fluxes in our model, and this does a good job describing the distribution of data from the EGS at high X-ray fluxes. At low X-ray fluxes, the predicted IR flux severely underestimates the average measured fluxes, in particular at  $3.6\mu\text{m}$ . This is because we do not include any emission from the host galaxy in our model SEDs. This will become important at the lowest AGN luminosities, especially at  $3.6\mu\text{m}$  where there will still be an important contribution from the old

stellar population of the galaxy. This problem does not seem to impact the  $8\mu\text{m}$  fluxes as strongly, but we will not be able to make accurate predictions at  $3.6\mu\text{m}$  or  $4.5\mu\text{m}$ . As seen in the following sections, this will not be a significant hindrance in producing strong predictions at longer wavelengths.

As evidence for this, Figure 10 plots the predicted 2–10 keV fluxes from the  $z < 3$  models in the 4:1/1pc and 4:1/10pc grids against the  $24\mu\text{m}$  flux. The symbols are the same as the previous plot except the red squares plot data from the CDFS presented by Alonso-Herrero et al. (2006). The locus of model predictions bisects the data points indicating that the calculated  $24\mu\text{m}$  flux gives a good description of an average AGN seen in the deep surveys. Also plotted in the figure are regions where bright local AGN (‘Piccionotti AGN’) and local starburst galaxies are expected to be found (see Alonso-Herrero et al. 2004, 2006). The  $N_{\text{H}}$ -weighted SEDs predict fluxes that place them within or on the lower boundary of the local AGN properties, again indicating that the models are good descriptions of AGN over a range of redshifts and luminosities.

In summary, the computed SEDs seem to adequately describe average AGN behavior from the X-ray to the mid-IR, a property that has previously only been possible using SED templates. These results also indicate that the assumption of a constant  $\alpha_{\text{ox}}$  is not resulting in a serious bias or error. Our computational approach has the advantage of being able to vary the physical properties of the absorbing gas to see which arrangement best describes the average AGN. The successful tests presented in this section validate this strategy and give confidence that the calculated number counts and LFs will have significant predictive power.

## 5. PREDICTIONS FOR BARE AGNS

This section presents the predicted cumulative number count distributions and luminosity functions resulting from the final  $N_{\text{H}}$ -averaged SEDs. Recall that our goal is to use the results of the deep hard X-ray surveys and the CXRB to predict the IR properties. Therefore, a key ingredient in computing these integrated quantities is the hard X-ray luminosity function (HXLF) and its evolution with  $z$  and  $L_X$ . As before (Ballantyne et al. 2006), we employ the luminosity-dependent density evolution HXLF of Ueda et al. (2003). This type of evolution has also been inferred by Hasinger et al. (2005) and La Franca et al. (2005) using other X-ray surveys.

### 5.1. Number Counts

The expression used to calculate the cumulative number counts at different IR wavelengths is the same as equation 3 from Ballantyne et al. (2006). However, an important difference in the calculation is that the integral over X-ray luminosity is begun at the minimum  $L_X$  that results in an IR flux  $S$ . In this way, for each IR wavelength of interest, number count distributions are computed for each of the three  $R$  evolutions considered, and for models with inner radii at 1 and 10 pc. Only the results with the simple  $N_{\text{H}}$  distribution are shown below, as there were only minor differences when the Risaliti et al. (1999) distribution was assumed.

Figure 11 plots the predicted cumulative number counts distributions at 5.7, 8, 24 and  $70\mu\text{m}$ . The black lines denote the three evolutions computed with the inner radius of the absorbing gas and dust at  $r = 1 \text{ pc}$  from the ionizing source, while the red lines show the results when  $r = 10 \text{ pc}$ . Within each color, the three line styles differentiate among the three evolutions of  $R$ . The data points in the 5.7, 8 and  $24\mu\text{m}$  panels

are the measured number counts of X-ray selected AGN from the GOODS survey (Treister et al. 2006).

In the  $5.7$  and  $8\mu\text{m}$  panels there are two dashed green lines that plot the computed number counts for the nozevol/ISM/1pc and nozevol/ISM/10pc models. The smaller grains included in the ISM model enhance the short wavelength IR emission, and therefore slightly increase the number counts at a given flux for these two *Spitzer* bands. This difference is small enough that it will not affect the arguments presented below.

It is clear from this figure that, apart from a small amount at  $24\mu\text{m}$ , there is little to no difference in the predicted number count distribution for the three evolutions of the type 2/type 1 ratio. This is a result of integrating over  $L_X$  and  $z$  which will tend to wash out any changes among the evolutionary models. Differences in the number count distributions do arise at  $70\mu\text{m}$ , but they are small in magnitude and it may be difficult for future surveys to reduce the errorbars to small enough values to discriminate among the different AGN evolutions.

The number count distributions do show a significant difference between the ones based on calculations with  $r = 1$  pc (black lines) and the models with  $r = 10$  pc (red lines). Before drawing conclusions it is important to consider the consequences of both our methodology and the observational selection effects on this plot. As mentioned above (Sect. 4.3), the omission of starlight from the host galaxy results in the models underpredicting the near-IR flux at low AGN fluxes. This will result in an underprediction of the number counts at small IR fluxes, with the difference increasing both in strength and in flux as we move to shorter wavelengths. The GOODS survey covers a small angle on the sky and the data plotted here are X-ray selected, so the survey will be missing both bright, rare objects and heavily obscured AGN, both of which are included in our calculations. Indeed, Donley et al. (2005) and Alonso-Herrero et al. (2006) both find that a significant fraction ( $\sim 50\%$ ) of AGN have been missed in the X-ray surveys, even at exposures  $> 1$  Ms (see also Ballantyne et al. 2006). The addition of rare, bright objects will result in the models overpredicting the number counts at the bright end. Compton-thick AGN, while very faint in the 2–8 keV X-ray band, can produce very typical AGN fluxes in the IR (Fritz et al. 2006). The inclusion of these sources in our models will result in an overprediction compared to the data points at all fluxes, where the amplitude of the error is related to the relative number of Compton-thick AGN.

With the above points in mind, Fig. 11 indicates that the  $r = 10$  pc models provide the best description of the observed number counts at all wavelengths. This is perhaps not surprising at observed-frame  $24\mu\text{m}$  as it is consistent with our earlier conclusions from Fig. 8 that the  $r = 1$  pc models do not on average produce enough  $24\mu\text{m}$  flux. However, this conclusion at observed-frame  $8\mu\text{m}$  seems at odds with Fig. 9 which indicates that the  $r = 1$  pc models are a better description of the  $8\mu\text{m}$  flux. With this interpretation, the number counts should be observed to be underpredicted by our models at low  $8\mu\text{m}$  flux, but this is only the case for the  $r = 10$  pc models. The two plots can be brought into agreement only if a non-AGN emission component begins to dominate the  $8\mu\text{m}$  flux below a certain X-ray flux. Indeed, the  $8\mu\text{m}$  flux of the EGS data is nearly constant below  $f_{0.5-10\text{ keV}} \sim 10^{-14} \text{ erg cm}^{-2} \text{ s}^{-1}$  (this is perhaps clearer in the original Fig. 7 of Barmby et al. 2006). Therefore, the  $r = 10$  pc models are consistent with both the EGS  $8\mu\text{m}$  fluxes and the  $8\mu\text{m}$  GOODS number counts.

To summarize this section, we have found that the cumulative number count distributions are very sensitive to the geometry of the obscuring material of the AGN, and the GOODS data are best described by the models where the attenuating material is  $\sim 10$  pc from the AGN. It will be interesting to compare these models to future AGN counts at  $70\mu\text{m}$ .

## 5.2. Luminosity Functions

As seen in Fig. 1, the three evolutions of  $R$  considered here predict very different values of the type 2/type 1 ratio with redshift. It is therefore expected that the redshift evolution of the IR luminosity functions should provide a means to discriminate among different evolutions of the AGN covering factor.

The Ueda et al. (2003) HXLF tells us how the number density of AGN per increment of  $\log L_X$  changes with  $z$  and  $L_X$ . The following expression is then used to convert this to an IR rest-frame LF  $d\Phi/d(\log \nu L_\nu)$  at a given wavelength,

$$\frac{d\Phi}{d(\log \nu L_\nu)} = \frac{d\Phi}{d(\log L_X)} \frac{d(\log L_X)}{d(\log \nu L_\nu)}. \quad (6)$$

As our photoionization technique allows a straightforward comparison between the hard X-ray and IR luminosities for each SED, the conversion factor in Eqn. 6 can be easily computed. As an example, Figure 12 plots the input 2–10 keV luminosity versus the IR luminosity for three different wavelengths using the results of the nozevol/1pc and nozevol/10pc grids. The range in IR luminosities is smaller than the range in the X-ray band, with the IR range decreasing with increasing wavelength. For example, at  $r = 1$  pc, although the X-rays span over 6 decades in luminosity, the resulting IR luminosity spans only about 5 decades at  $15\mu\text{m}$  and 4 decades at  $30\mu\text{m}$ . This wavelength-dependent sensitivity on the input X-ray luminosity is a result of our specific source geometry and the resulting amounts of dust available to emit at the different IR energies. Emission at shorter IR wavelengths is dominated by hot dust, and as the luminosity of the ionizing source increases, greater amounts of dust are raised to high temperature. The longer wavelengths are dominated by cooler dust, but as the luminosity increases our models may truncate the illuminated cloud before large amounts of this dust are warmed. This behavior is confirmed in Sect. 7.4, where we show that a reduction in the density of the IR-emitting region, and an accompanying increase in its size, can significantly increase the long wavelength output of the model at high  $L_X$ .

The factor  $d(\log L_X)/d(\log \nu L_\nu)$  used in eq. 6 is of course the slope of the lines plotted in Fig. 12. At a given  $z$  and wavelength, the IR LFs are then computed for each evolutionary model by iterating over  $L_X$ , finding the appropriate IR luminosity, determining the slope  $d(\log L_X)/d(\log \nu L_\nu)$  at that luminosity, and then multiplying the HXLF at  $(L_X, z)$  by that slope. As with the number count distributions, the results described below assume the simple  $N_H$  distribution as described in Sect. 2.

The predicted rest-frame  $8\mu\text{m}$  LFs for the three  $R$  evolutions are plotted<sup>5</sup> in Figure 13 at  $z = 0.2, 0.6$  and  $2.0$ . The left- and right-hand panels show the  $r = 1$  and  $10$  pc results, respectively. To emphasize any differences among the LFs, the lower window in each panel shows, for each of the three redshifts, the ratio between the evolving LFs and non-evolving LF. It is clear that the LFs do allow a mechanism to

<sup>5</sup> These LFs and the others at longer wavelengths were computed using the results from grids with Orion grains. LFs computed with ISM grains made a negligible difference, even at  $8\mu\text{m}$ , and therefore are not presented.



determine among the different evolutionary scenarios for the AGN type 2/type 1 ratio. If the inner radius of the attenuating gas and dust is on average  $\sim 1$  pc from the AGN, then, at  $z = 0.2$ , both the 1:1 and 4:1 evolving models predict  $8\mu\text{m}$  LFs smaller than the non-evolving case by factors greater than 2 for objects just past the knee of the LF. At higher  $z$ , the large fraction of type 2 objects predicted by the 1:1 evolutionary model (see Fig. 1(b)) results in a factor  $> 3$  enhancement of the LF over the non-evolving model. If the obscuring material has an inner radius of  $\sim 10$  pc then these differences move to higher luminosities and, at low  $z$ , reduce in amplitude. This is because when the gas is further away larger AGN luminosities are needed to produce the hot dust emission at  $8\mu\text{m}$ .

The data points in Fig. 13 are the measured type 1 AGN LF at  $z = 2$  from Brown et al. (2006). These objects were observed at  $24\mu\text{m}$  and lie at  $1 \leq z \leq 5$  and therefore correspond to rest-frame emission at  $4\text{--}12\mu\text{m}$ . It is obvious that the  $z = 2$  LFs computed with  $r = 10$  pc provide a better match to the observed LF than the ones computed with  $r = 1$  pc, consistent with the conclusion on  $r$  reached by considering the number counts (Sect. 5.1). The close match in amplitude between the predicted and measured LFs is probably fortuitous, as the computed LF is for both type 1 and type 2 AGNs computed at one  $z$ , while the measurements are for only type 1s spread over a large range of  $z$ . Nevertheless, the agreement in the shape of the LF with the  $r = 10$  pc models is significant.

To explore the behavior of the absorbing material at longer wavelengths, we plot in Figure 14 the predicted LFs for rest-frame  $30\mu\text{m}$ . The differences among the three evolutions are enhanced at this longer wavelength, with both the evolving models underpredicting the  $z = 0.2$  non-evolving LF by factors  $> 10$ . Moreover, for both the  $r = 1$  and  $10$  pc set of models the differences persist over a much larger range of luminosity than at  $8\mu\text{m}$ . At  $z = 1$ , the large number of obscured AGN predicted by the 1:1 evolution leads to an enhancement of the  $30\mu\text{m}$  LF by factors that can approach 50 if  $r = 1$  pc or 100 if  $r = 10$  pc. The largest differences among the evolutions appear above the knee of the LFs and move to higher luminosities in the  $r = 10$  pc models. Evidently, the warm dust emission is very sensitive to the covering factor of gas around the AGN, and therefore provides a clear tracer of any evolution with  $z$ .

In order to compare these computed  $30\mu\text{m}$  LFs to data we made use of the SWIRE survey of Franceschini et al. (2005). These authors presented AGN SEDs from *Spitzer* IR to optical and X-ray wavelengths for X-ray detected AGN in the ELAIS N1 region. Using their SEDs, we estimated the  $60\mu\text{m}$  flux density and computed the rest-frame  $30\mu\text{m}$  LF at  $z = 1$ . The LF was derived by the  $1/V_{\text{max}}$  method. The redshift distribution of sources peaks around  $z \sim 1$  and the derived LF is not sensitive to the choice of the redshift bin. A redshift bin of 0.8–1.2 was selected in order to ensure a reasonable number of objects (the LF changes by  $< 20\%$  for a redshift bin 0.9–1.1). The range of  $30\mu\text{m}$  luminosity,  $\nu L_\nu$ , of objects at  $0.8 < z < 1.2$  is about one order of magnitude and we employed a range of  $\nu L_\nu = 10^{44}\text{--}10^{44.5}$  erg s $^{-1}$  to exclude an outlier. For simplicity, we assume the same incompleteness over both the redshift and luminosity bins, although this can result in overestimating the LF. However, the LF without the incompleteness correction is smaller by only 30%, within the estimated uncertainty. Corrections were made for the 99% completeness of X-ray detection (see Manners et al. 2003), the 90% completeness of infrared source detection, and the identification of 102/122 X-ray sources in the *Spitzer*

IRAC image. The uncertainty of the LF includes the Poisson noise statistics on the number of sources and the uncertainty in the observed  $30\mu\text{m}$  luminosity estimated by fitting the SEDs. While the IR SED fitting is based on the IRAC data, most of the objects used for constructing the LF also have  $24\mu\text{m}$  detections and they are roughly consistent with the SED fitting. The  $f_{25\mu\text{m}}/f_{12\mu\text{m}}$  ratio of local ( $z < 0.2$ ) Seyfert galaxies varies only by a factor of  $\sim 3.5$  (Neugebauer et al. 1986). Thus, we argue that this factor is a conservative estimate of the uncertainty in the observed  $30\mu\text{m}$  luminosity, because the IR SED fitting performed by Franceschini et al. (2005) is based on IR data points at several wavelengths. The final LF is plotted in Figure 14, where the uncertainty is dominated by the uncertainty in the IR luminosity.

This datapoint is consistent with the predictions of the  $r = 1$  and  $r = 10$  pc models. If the rest-frame  $30\mu\text{m}$  emission from an average AGN with this luminosity at  $z = 1$  arises from material with an inner radius of  $\sim 1$  pc from the central source, then only the 1:1 evolution predicts enough absorbed AGN to account for the observed LF. Converting the IR luminosity of this data point to an X-ray luminosity gives  $\log L_X \approx 44$ . At this luminosity and  $z = 1$ , Fig. 1 shows that evolution 4 predicts a type 2/type 1 ratio of  $\sim 5:1$ , as opposed to the  $\sim 2:1$  ratio derived from the other two models. These lower ratios are consistent with the data point if the inner radius of the absorbing gas and dust is at  $10$  pc. Unfortunately, in this situation the luminosities of the AGN are too low to distinguish among the three evolutions.

Moving to even longer wavelengths further enhances the differences among the three different models of  $R(L, z)$ , although complications arising from star formation are more important at longer wavelengths (see next section). The rest-frame  $35\mu\text{m}$  LF, which is accessible to *Spitzer* at  $z = 1$  using the  $70\mu\text{m}$  MIPS band exhibits a similar behavior as seen at  $30\mu\text{m}$  with the differences in the LFs increased to factors  $\sim 100$  at both  $z = 0$  and  $1$ .

## 6. ACCOUNTING FOR STAR FORMATION

In the previous section we found that large differences among the three type 2/type 1 evolutions are found at  $30\mu\text{m}$  (for both the  $1$  pc and  $10$  pc models). However, these longer wavelengths will likely be contaminated with emission from star-forming regions. This will be particularly troublesome at  $z \sim 1$  if the AGN absorbing gas is connected to the SFR in the host galaxy. Therefore, some limits need to be placed on the effects of star-formation on the above predictions.

A simple way to proceed is to make use of the work of Yun & Carilli (2002), who fit a single temperature dust model to the far-IR/sub-mm emission of local starburst galaxies (they also included bremsstrahlung and synchrotron emission, but emission from these processes is only important at much longer wavelengths). The median dust temperature  $T_d$  and emissivity index  $\beta$  they find from their sample is  $T_d = 58$  K and  $\beta = 1.35$ . By relating the total  $40\text{--}500\mu\text{m}$  emission to the SFR by  $\text{SFR} = L_{40\text{--}500\mu\text{m}} / (5.8 \times 10^9 L_\odot) M_\odot \text{ yr}^{-1}$ , Yun & Carilli (2002) then write the dust emission as

$$L_\nu = 1.56 \times 10^{21} \nu^3 \text{SFR} \frac{(1 - e^{-(\nu/2000)^{1.35}})}{(e^{0.00083\nu} - 1)} \text{ erg s}^{-1} \text{ Hz}^{-1}, \quad (7)$$

where  $\nu$  is in GHz.

As this spectrum assumes only one relatively cool dust temperature and ignores more complicated dust physics such as PAH emission and non-linear temperature spiking from very-

small grains, it will not be an accurate correction to the AGN spectra at wavelengths  $\lesssim 20\mu\text{m}$ . It should be a reasonable correction at  $30\mu\text{m}$ . The dust emission spectrum (Eq. 7) was added to the final  $N_{\text{H}}$ -averaged Cloudy SEDs between 3 and  $1500\mu\text{m}$  assuming constant SFRs of 0.5, 1, 5, 10 and  $100 M_{\odot} \text{ yr}^{-1}$ .

As the number count distributions did not provide a good method to discriminate among the three evolutionary models, we will omit a discussion on how star-formation impacts the number counts. Suffice it to say that the only non-negligible effect on the predicted distributions occurs at  $70\mu\text{m}$ .

Turning to the LFs, Figure 15 plots how one particular  $30\mu\text{m}$  luminosity function is altered by adding in dust emission from the different SFRs. For SFRs  $\leq 10 M_{\odot} \text{ yr}^{-1}$  significant deviations occur only when  $\log \nu L_{\nu} \gtrsim 44.5$ . At low AGN luminosities the majority of the  $30\mu\text{m}$  emission is from the star-formation emission. In contrast, the  $30\mu\text{m}$  LF can be dramatically changed at nearly all luminosities if the SFR  $\sim 100 M_{\odot} \text{ yr}^{-1}$ . When the SFR reaches these values, the  $30\mu\text{m}$  luminosity is only mildly sensitive to the heating from the AGN. Although there is significant scatter from object to object, such a high SFR seems to be reached in an average galaxy only at  $z \gtrsim 1.5$  (Juneau et al. 2005; Papovich et al. 2006). However, in spite of the changes to the  $30\mu\text{m}$  LF caused by star-formation, Figure 16 shows that the LFs from the three AGN type 2/type 1 ratios are still significantly different for SFRs  $\leq 10 M_{\odot} \text{ yr}^{-1}$ , and the discussion from the previous section is still valid. This figure does suggest, however, that generating a LF from sources with a lower SFR would be preferable.

## 7. DISCUSSION

The goal of this paper was to investigate how three possible evolutions of the AGN type 2/type 1 ratio (all of which fit the CXRB) manifest themselves in the mid-IR. The predictions were computed by employing the photoionization code Cloudy to calculate the SED from an obscured AGN over a large range of X-ray luminosity,  $L_X$ , and redshift. In this way, a direct connection between the observed X-ray and IR fluxes could be predicted. The covering factor of the absorbing gas and dust changed with  $z$  and  $L_X$  as predicted by CXRB synthesis models and the unified model.

The results presented in the above two sections show that this photoionization-based method is very successful. The family of computed SEDs indeed capture many of the average properties in typical AGN observed in the deep surveys of *Chandra*, *Spitzer* and *XMM-Newton*, including infrared colors and observed IR and X-ray fluxes. Typically, investigations of the IR properties of AGN involve either detailed dust radiative transfer models (e.g., Granato et al. 1997) that provide no connection to the X-rays, or are based on phenomenological SEDs and are unable to provide constraints on physical parameters (e.g., Silva et al. 2004). Our approach is not designed to fit the SEDs of individual objects, but we can use it to constrain physically interesting quantities in the ensemble of objects. In this way, a picture of an average AGN can emerge, uncluttered from the significant source-to-source variability that affects the study of small samples.

### 7.1. The Location of the Absorbing Gas

Two different inner radii were used in computing the Cloudy models, 1 pc and 10 pc (see § 3.3), as tests for whether large samples of AGN show evidence for dust emission at these average distances. Although only these two radii were

considered here, comparing the results from the two sets of models with the available data gave rise to the interesting result that almost all observational tests preferred the 10 pc models over the 1 pc ones (Figs. 3 and 8). In particular, the GOODS number-count distributions were best described by the 10 pc models from observed-frame  $5.7\mu\text{m}$  to  $24\mu\text{m}$  (Fig. 11).

It is important to note here that both the  $r = 1$  and 10 pc sets of models were assumed to have the same constant density of  $10^4 \text{ cm}^{-3}$ . Thus, all Cloudy runs with  $\log N_{\text{H}} < 23.5$  have pathlengths less than 10 pc (ignoring ionization effects). As a result the  $r = 1$  pc models will be dominated by hot dust, as the column does not extend to great enough distances to produce significant warm emission. A new lower density distribution that would have an inner radius of 1 pc and be able to produce the correct  $24\mu\text{m}$  flux is certainly conceivable. On the other hand, if the obscuring medium is clumpy with each clump being roughly the same density (Dullemond & van Bemmelen 2005), then our setup may not be too unrealistic. An investigation using different density distributions will be the subject of future work.

Although the 10 pc model seems to be the best description of data observed at the mid-IR *Spitzer* wavelengths, the observed SEDs of many AGN show that hot dust from inside this radius is also required. The 10 pc Cloudy models do predict dust temperatures close to and at the sublimation value at the inner radius of the cloud, but only for the more luminous AGN models (see § 3.3). Thus, there must be dust emission over a range of radii and temperatures, in agreement with SED fitting of individual objects (e.g., Kuraszkiwicz et al. 2003). This conclusion is also consistent with observations searching for variability in the IR continua of AGN that find little to no variations at mid- to far-IR wavelengths on day to month long timescales (Rieke & Lebofsky 1981; Edelson & Malkan 1987; Clement et al. 1988). In contrast, near-IR (JHK band) variability of local Seyferts is observed with measured timelags from the optical/UV placing the emitting region  $< 1$  pc from the continuum source (Clavel et al. 1989; Suganuma et al. 2006; Minezaki et al. 2006).

Neugebauer & Matthews (1999) report long term monitoring of nearby, low-luminosity quasars at  $10.6\mu\text{m}$ . At the typical redshifts of their sample, this wavelength is very close to  $8\mu\text{m}$  in the rest-frame. They find slow, multiple-year variability but conclude that in no case are the results in contradiction to a thermal origin for the emission in the objects with luminosities  $< 10^{13} L_{\odot}$ . Specifically, the variability time scales are consistent with our conclusion that the  $8\mu\text{m}$  emission arises from thermal re-radiation by dust in a component with a typical inner radius of  $\sim 10$  pc. They also summarize previous measurements of luminous, radio-loud quasars, such as 3C 273; in this object in particular, observations at  $\sim 8\mu\text{m}$  in the rest frame show variations that are too fast to interpret as thermal radiation. Since such objects are exceptional among the total quasar population, it is unlikely that such behavior would strongly affect our results for the ensemble properties of these sources.

In the future, model grids can be extended to even larger inner radii to establish a pair of bracketing values for this key parameter. It will also be possible to break observed data into redshift and luminosity slices to determine if there is an evolution of the inner radius with  $z$  and/or  $L_X$  (e.g., Hatziminaoglou et al. 2006).

### 7.2. Determining the Evolution of $R$

Sections 5 and 6 showed that the mid-IR LF of AGN will be able to discriminate among different models of  $R$ , the type 2/type 1 ratio. Out of the wavelengths considered here, the rest frame  $30\mu\text{m}$  LF between  $z = 0$  and 1 gives the largest differences among evolutionary scenarios, as well as being the least contaminated due to star-formation emission. This last point needs to be confirmed with a more sophisticated prediction of the IR emission due to star-formation.

Assuming the 10 pc models are a more accurate guide, then the right-hand panel of Fig. 14 indicates that largest differences among evolutions of  $R$  occurs at luminosities with  $\log \nu L_\nu > 45$ . This is past the knee of the LF, and so will require wide surveys to pick up the large numbers of luminous AGN. The observations will also require significant depth in order to trace the LF out to  $z \sim 1$ .

Another issue in observationally testing the LF predictions is accessible wavebands. To really understand the evolution of the obscuring region, one would like to trace the LF from low redshift (say,  $z = 0.2$ ) to  $z \sim 1$ . The LF predictions are in the rest-frame, which means that for  $30\mu\text{m}$  observations at  $z \sim 0.6$ , the required flux is being radiated at  $48\mu\text{m}$ . One would then be forced to perform multi-wavelength observations and SED fitting for each object in order to predict the flux at the required wavelength. This SED fitting could be relatively simple as the largest uncertainties for determining the LF will be in the space density statistics.

Given these difficulties, it is natural to ask if the mid-IR LF is the easiest method to determine the evolution of  $R$ . A perhaps more straightforward strategy would be to measure the ratio of narrow-line to broad-line AGN in the optical as functions of  $z$  and  $L_{[\text{O III}]}$ , the luminosity in the  $[\text{O III}] \lambda 5007$  line. Alternatively, we could measure the ratio of X-ray AGN with absorbing column densities  $\log N_{\text{H}} < 22$  to those with  $\log N_{\text{H}} > 22$  as a function of  $z$  and  $L_X$ , although an accurate value of  $N_{\text{H}}$  requires an X-ray spectrum with sufficient counts. Since it is currently difficult to obtain enough counts for spectral fitting from faint sources, hardness ratios (which assume a spectral slope) are often used as an alternative. Thus, both of these other methods to track the evolution of  $R$  require serious observational investments, but, more problematically, they also are both subject to severe selection effects. As is becoming increasingly apparent, optical selection of AGN (i.e., selection on the basis of high-ionization lines) has significant limitations (e.g., Netzer et al. 2006) and many (mostly type 2 AGN) are missed due to obscuration or dilution (Moran et al. 2002; Eckart et al. 2006; Rigby et al. 2006). Likewise, X-ray selection is limited because the observable passband for the most sensitive telescopes ends at  $\sim 10$  keV, and the observations are thus insensitive to objects with high column densities, especially those with  $N_{\text{H}} > 10^{24} \text{ cm}^{-2}$ , the Compton-thick AGN. The high energy detectors on *Swift* and *Integral* have been able to conduct surveys, but are limited to the nearby Universe due to low sensitivity (Markwardt et al. 2005; Bassani et al. 2006). Future observations with the Hard X-ray Detector on board *Suzaku* may help, but it is a non-imaging instrument. The cancellation of the hard X-ray imaging mission *NuStar* makes finding significant numbers of the Compton-thick AGN by their hard X-ray emission practically impossible until the launch of *Constellation-X*.

The advantage of the mid-IR method described here is that it is less affected by the above selection effects. The predicted LFs shown in Fig. 14 are for both type 2 and type 1 AGN, therefore detailed optical emission line spectra are not required. Compton-thick objects should also be found in the

infrared, as the absorbed X-ray radiation will be re-emitted by the dust. The difficulty, of course, is determining which IR sources are predominantly powered by AGN as opposed to star-formation, although methods that examine the spectral shape of the near- and mid-IR have had some success (Alonso-Herrero et al. 2006; Brand et al. 2006), and AGN are well known to have very weak PAH emission (Weedman et al. 2005). However, X-ray selection is still the best way to identify AGN, as Compton-thin objects can be observed to high redshifts. Deep infrared observations are then required to find the Compton-thick sources. Comparisons between multiband observations and simulations similar to those performed here will be useful in determining the AGN contribution to these potential Compton-thick sources. This can be done by adding in contributions from the host galaxy to the photoionization models, and computing a large grid of IR properties over a range of AGN luminosities and redshifts for comparison to both near- and mid-IR data.

Another interesting effect seen in the IR and not in the other wavelengths is the dependence on the geometry of the obscuring medium. Figures 13 and 14 have shown different shapes for the LF depending on the inner radius of the absorbing gas and dust. For the one data point at  $30\mu\text{m}$ , it was difficult to determine the best evolution of  $R$  without knowing the geometry. Fortunately, there are significant differences in the predicted LFs and number counts for the different inner radii. Therefore, it is possible to break the degeneracy between  $r$  and  $R$ , as was done at rest-frame  $8\mu\text{m}$  (Fig. 13).

Finally, the mid-IR LFs presented above are relatively insensitive to the actual  $N_{\text{H}}$  distribution assumed. We considered both a ‘simple’  $N_{\text{H}}$  distribution, where all column densities had equal weight within the type 1 or 2 designations (eqn. 1), and the Risaliti et al. (1999)  $N_{\text{H}}$  distribution in which half of the type 2 AGN are Compton thick and 75% had  $\log N_{\text{H}} > 23$  (eqn. 2). These weights were used in constructing both the ‘unified’ and  $N_{\text{H}}$ -averaged SEDs. Despite this, the two distributions made only negligible differences to the predicted number counts and LFs. This is because the additional weight afforded to Compton thick AGN in the Risaliti et al. (1999)  $N_{\text{H}}$  distribution has only a small effect in the mid-IR (Fig. 2). Therefore, although mid-IR LFs will not be able to quantify the relative number of Compton thick AGN, they are still very sensitive to the overall evolution of the AGN type 2/type 1 ratio.

### 7.3. The Role of Star Formation

Star formation is a key process in this investigation in two distinct ways. First, it acts as a contaminant of the mid-IR emission from the obscured AGN, masking the evolutionary effects we are trying to investigate. Using a straightforward estimate of the effects of star formation on the mid-IR, we found in Sect. 6 that for a constant SFR  $\leq 10 M_\odot \text{ yr}^{-1}$  the impact at  $30\mu\text{m}$  was confined to  $\log \nu L_\nu < 44.5$ , which translates to X-ray luminosities of  $\log L_X \lesssim 43.5$  for the 1:1/10pc models or  $\log L_X \lesssim 43.7$  for the nozevol/10pc and 4:1/10pc grids. The affected luminosities are low enough that the rest-frame  $30\mu\text{m}$  LFs may still be used to discriminate possible different evolutions of the AGN type 2/type 1 ratio (Fig. 15). The method may prove more problematic with galaxies with average SFRs  $> 10 M_\odot \text{ yr}^{-1}$ .

The sources that produce the majority of the CXRB have been identified to be predominantly obscured AGN with  $43 \leq \log L_X \leq 44$  (Barger et al. 2005). These objects are typically found at  $z \lesssim 1$ , which may signify a relationship between

the obscuring material around an AGN and the star formation in the host galaxy (Fabian et al. 1998; Franceschini et al. 1999; Ballantyne et al. 2006). It is this possibility that makes measuring the evolution of  $R$  an important goal in the study of galaxy evolution. However, there may be a potential difficulty in employing the mid-IR LFs calculated here because, as already noted, the important luminosity range to distinguish the various evolutions is  $\log L_X \gtrsim 44$ , larger than that of the objects that dominate the X-ray background. The reason for this is that the three evolutions considered have very different predictions for the ratio of type 2/type 1 quasars (Fig. 1), but quasars probably have a very different formation and evolution history than the lower luminosity Seyferts that comprise the bulk of the CXRB. Quasars are more commonly found at  $z \gtrsim 1$ , are likely formed by the mergers of massive galaxies, and simulations show their host galaxies have little ongoing star formation within the galaxy at late times (e.g., Hopkins et al. 2005). The evolutions of  $R$  described by eqns. 3 and 4 assume that the AGN covering factor increases with  $z$  independent of the AGN luminosity. If the attenuating gas and dust is connected to the host galaxy SFR then this may not be correct at large  $L_X$ , and indeed very tentative evidence for a slower increase of  $R$  with  $z$  at larger  $L_X$  was found by Ballantyne et al. (2006). If this is the case, then evidence for this type of luminosity-dependent redshift evolution will appear in the  $30\mu\text{m}$  LFs, and can be measured using the techniques presented here. Furthermore, the effects of our luminosity-independent assumption are most important at high  $z$ , but Fig. 14 show that significant variations in the rest-frame  $30\mu\text{m}$  LF due to the different evolutions of  $R$  still occur at low redshifts. Thus, a determination of the LF at redshifts  $z \sim 0-0.2$  will result in an important constraint on the local value of  $R$ . Then, tracking the  $30\mu\text{m}$  LF with redshift will yield a measurement of how the AGN type 2/type 1 ratio changes with  $z$  and  $L_X$ , a key parameter in understanding the formation and evolution of these galaxies.

#### 7.4. Testing the Unified Model

To this point, all the calculations presented in this paper assumed that the unified model of AGN was correct. That is, the fraction of type 2 AGN at a given  $L_X$  and  $z$  is equal to the covering factor of the absorbing material around the AGN. These models can also be used to test whether the unification scenario is valid at all luminosities.

As an example, we searched for *IRAS* objects satisfying  $|b| > 35$  degrees,  $f_\nu(60\mu\text{m}) > 0.2$  Jy and with redshifts between 0.8 and 1.2. This results in 13 objects in which we identified 8 quasars using the literature. Two of them ([HB89]0235+164 and [HB89]1308+326) are blazars and are omitted from further consideration. An additional 3 (*IRAS* F09121+2430, PG1248+401 and B31340+407) were removed because they have weak detections at  $60\mu\text{m}$  and the association with the quasars therefore is not firmly established. The remaining three quasars (2MASSJ0119560-201022, 2MASSJ1543519+162422 and PG1206+459) have strong detections by *IRAS* and the optical data show them to have normal QSO SEDs. Assuming  $z \sim 1$ , the rest-frame  $30\mu\text{m}$  luminosities of these quasars are  $\nu L_\nu \sim 46.8$ . Fig. 14 shows that the 1:1/10pc evolutionary model, as a result of its  $\sim 3:1$  type 2/type 1 ratio (Fig. 1), can reach a  $30\mu\text{m}$  luminosity of  $\nu L_\nu = 46.5$  at  $z = 1$ , but this occurs only when the input X-ray luminosity is  $\log L_X = 48$ . Yet, the 2–10 keV X-ray luminosity of PG1206+459 is  $\sim 10^{45}$  erg s $^{-1}$  (Piconcelli et al. 2005). Indeed, using the three *IRAS* sources

to estimate the  $30\mu\text{m}$  LF at  $\nu L_\nu = 46.8$  results in a lower-limit of  $> 10^{-10}$  Mpc $^{-3}$ , about 2 orders of magnitude larger than the predicted LF from Fig. 14. The best way of reducing this discrepancy would be if the models could produce these high IR luminosities at lower AGN input luminosities.

It seems that the assumed geometric configuration of a relatively compact absorbing medium situated at 1 pc or 10 pc from the AGN cannot produce the necessary  $30\mu\text{m}$  emission at high  $L_X$  to account for the *IRAS* limit. Recall that because of the assumed density of  $10^4$  cm $^{-3}$ , the pathlength through the absorber is only 15 pc for  $\log N_H = 23$  and  $\log L_X = 48$  (taking into account the ionization effects), therefore at high AGN luminosities there is only a small column of dust cool enough to emit at  $30\mu\text{m}$ . Material at greater distances is needed to increase the  $30\mu\text{m}$  emission. A simple way to test this idea is to calculate a new grid of *Cloudy* models with the inner radius remaining at 10 pc but the density now lowered to  $10^2$  cm $^{-3}$ . This greatly increases the pathlength of the absorbing material (it is now over 1 kpc in the example above). Figure 17 plots the rest-frame  $30\mu\text{m}$  LFs computed using the models with a lower density absorber as well as the previous derived ones that assume the more compact geometry. Only results for  $\log \nu L_\nu \gtrsim 44.7$  are plotted for the low density absorber. The greater pathlength afforded by the lower density cloud now produces enough  $30\mu\text{m}$  emission to account for the *IRAS* lower-limit. The right-hand panel of Fig. 17 shows the same results but for the rest-frame  $8\mu\text{m}$  LF. At this wavelength, the differences in the LF between the two assumed densities are small.

The implication of this simple test is that the high luminosity quasars require absorption and remission of nuclear radiation over a large range of radii, while the current data available for the lower luminosity quasars and Seyfert galaxies can be adequately described by a more compact absorber. The type 2/type 1 ratio at the *IRAS* luminosities for the three evolutions considered in this paper varies from  $\sim 1:1-4:1$  (Fig. 1), a range that is consistent with the latest observational constraints (Martínez-Sansigre et al. 2005, 2006). Under the unification model, this translates into covering fractions of 0.5–0.8. Producing high covering fractions is significantly simpler if the obscuring material is close to the AGN, and not spread out over a large range of radii, as implied by the above results. Clearly, the change in mid-IR LF with luminosity (in addition to the possible redshift evolution concentrated on in previous sections) contains fundamental clues on the nature and geometry of the obscuring medium and therefore the host galaxy. Future observations are needed for this technique to fulfill this promise.

We conclude that the unification model based on a relatively compact absorber is consistent with the available data for moderate AGN luminosities (Seyfert galaxies) but fails when extending this to the high luminosity quasars. This adds to the evidence that the evolution and fueling of quasars are very different from those that drive the lower luminosity Seyfert galaxies.

## 8. SUMMARY

The principle conclusion of this work is that a measurement of the redshift evolution of the mid-IR AGN LF will determine to what extent the AGN type 2/type 1 ratio,  $R$ , is evolving with  $z$ . The specific predictions shown above were of most use for the existing *Spitzer* MIPS bands, but are equally valid for future observations with *JWST*. Predictions were shown for three different evolutions of  $R$ , but the current

data were unable to distinguish among them.

The calculations performed here were relatively novel, as they employed the photoionization code Cloudy to directly connect the X-ray properties of AGN to the IR. This technique, although not appropriate for fitting SEDs of individual objects, yielded  $N_{\text{H}}$ -averaged SEDs that well described the average properties of AGN found in the deep surveys. In addition, varying the parameters of the models allows constraints to be placed on the physical conditions for an average AGN absorber. For example, comparing results assuming two different distances for the average inner radius of the attenuating gas and dust (1 pc and 10 pc), yielded compelling evidence that the rest frame mid-IR properties of a large ensemble of AGN were best described when the inner radius of the obscuring material was  $\sim 10$  pc from the AGN. Future work will cover a greater parameter space and split the data into both redshift and luminosity bins. In this way, properties of average AGN can be derived and followed with minimal interference from the intrinsic object-to-object variability.

Finally, it is worth emphasizing the importance of determining the evolution of the AGN type 2/type 1 ratio, as it may be directly related to processes within the host galaxy. Between  $z \sim 0$  and 1, most AGN are relatively low-luminosity Seyfert galaxies and therefore such studies probe a differ-

ent mode of galaxy formation and evolution than the higher-luminosity quasars at high redshifts. Evidence for such a difference was uncovered by estimating the rest-frame  $30\mu\text{m}$  LF at high quasar luminosities. This LF was more than two orders of magnitude above the predictions, which assumed that a compact unification model was valid at all luminosities. To account for this observational limit absorbing material at much larger radii was invoked, suggesting a different mode of obscuration. Seyfert galaxies, in contrast, can still be successfully described by the compact unified model.

This research has made use of the NASA/IPAC Extragalactic Database (NED) which is operated by the Jet Propulsion Laboratory, California Institute of Technology, under contract with the National Aeronautics and Space Administration. DRB is supported by the University of Arizona Theoretical Astrophysics Program Prize Postdoctoral Fellowship. Partial support for this work was provided by NASA through a contract 1255094 issued by JPL/Caltech. We thank G.J. Ferland for providing the community with Cloudy, D. Psaltis for allowing us to use the Sierra cluster for the computations, and J. Everett for comments on a draft of the paper.

## REFERENCES

- Alonso-Herrero, A., Quillen, A.C., Rieke, G.H., Ivanov, V.D. & Efstathiou, A., 2003, *AJ*, 126, 81  
 Alonso-Herrero, A. et al., 2004, *ApJS*, 154, 155  
 Alonso-Herrero, A. et al., 2006, *ApJ*, 640, 167  
 Andreani, P., Cristiani, S., Grazian, A., La Franca, F. & Goldschmidt, P., 2003, *AJ*, 125, 444  
 Antonucci, R., 1993, *ARA&A*, 31, 473  
 Ballantyne, D.R., Weingartner, J.C. & Murray, N., 2003, *A&A*, 409, 503  
 Ballantyne, D.R., Everett, J.E. & Murray, N., 2006, *ApJ*, 639, 740  
 Barger, A.J., Cowie, L.L., Brandt, W.N., Capak, P., Garmire, G.P., Hornschemeier, A.E., Steffan, A.T. & Wehner, E.H., 2002, *AJ*, 124, 1839  
 Barger, A.J., Cowie, L.L., Mushotzky, R.F., Yang, Y., Wang, W.-H., Steffan, A.T. & Capak, P., 2005, *AJ*, 129, 578  
 Barmby, P. et al., 2006, *ApJ*, 642, 126  
 Barvainis, R., 1987, *ApJ*, 320, 537  
 Bassani, L. et al., 2006, *ApJ*, 636, L65  
 Brand, K. et al., 2006, *ApJ*, 644, 143  
 Brandt, W.N. & Hasinger, G., 2005, *ARA&A*, 43, 827  
 Brown, M.J.I. et al., 2006, *ApJ*, 638, 88  
 Buchanan, C.L., Gallimore, J.F., O’Dea, C.P., Baum, S.A., Axon, D.J., Robinson, A., Elitzur, M. & Elvis, M., 2006, *AJ*, 132, 401  
 Clavel, J., Wamsteker, W. & Glass, I.S., 1989, *ApJ*, 337, 236  
 Clement, R., Sembay, S., Hanson, C.G. & Coe, M.J., 1988, *MNRAS*, 230, 117  
 Davies, R.I. et al., 2006, *ApJ*, in press (astro-ph/0604125)  
 De Luca, A. & Molendi, S., 2004, *A&A*, 419, 837  
 Donley, J.L., Rieke, G.H., Rigby, J.R. & Pérez-González, P.G., 2005, *ApJ*, 634, 169  
 Dullemond, C.P. & van Bemmell, I.M., 2005, *A&A*, 436, 47  
 Eckart, M.E., Stern, D., Helfand, D.J., Harrison, F.A., Mao, P.H. & Yost, S.A., 2006, *ApJS*, 165, 19  
 Edelson, R.A. & Malkan, M.A., 1987, *ApJ*, 323, 516  
 Efstathiou, A. & Rowan-Robinson, M., 1995, *MNRAS*, 273, 649  
 Fabian, A.C., Barcons, X., Almaini, O. & Iwasawa, K., 1998, *MNRAS*, 297, L11  
 Fadda, D., Giuricin, G., Granato, G.L. & Vecchies, D., 1998, *ApJ*, 496, 117  
 Ferland, G.J., 2003, *ARA&A*, 41, 517  
 Ferland, G.J., Korista, K.T., Verner, D.A., Ferguson, J.W., Kingdon, J.B., & Verner, E.M., 1998, *PASP*, 110, 761  
 Franceschini, A., Hasinger, G., Miyaji, T. & Malquori, D., 1999, *MNRAS*, 310, L5  
 Franceschini, A. et al., 2005, *AJ*, 129, 2074  
 Fritz, J., Franceschini, A. & Hatziminaoglou, E., 2006, *MNRAS*, 366, 767  
 Gilli, R., 2004, *Advances in Space Research*, 34, 2470  
 Gilli, R., Risaliti, G. & Salvati, M., 1999, *A&A*, 347, 424  
 Gilli, R., Salvati, M. & Hasinger, G., 2001, *A&A*, 366, 407  
 Granato, G.L. & Danese, L., 1994, *MNRAS*, 268, 235  
 Granato, G.L., Danese, L. & Franceschini, A., 1997, *ApJ*, 486, 147  
 Hao, L., et al., 2005, *AJ*, 129, 1795  
 Hasinger, G., Miyaji, T. & Schmidt, M., 2005, *A&A*, 441, 417  
 Hatziminaoglou, E. et al., 2006, in *Infrared Diagnostics of Galaxy Evolution*, ASP Conf. Ser., in press (astro-ph/0603359)  
 Ho, L.C., Filippenko, A. & Sargent, W.L.W., 1997, *ApJ*, 487, 568  
 Hopkins, A.M., 2004, *ApJ*, 615, 209  
 Hopkins, P.F., Hernquist, L., Cox, T.J., Di Matteo, T., Martini, P., Robertson, B. & Springel, V., 2005, *ApJ*, 630, 705  
 Juneau, S. et al., 2005, *ApJ*, 619, L135  
 Khachikian, E.Ye. & Weedman, D.W., 1974, *ApJ*, 192, 581  
 Königl, A. & Kartje, J.F., 1994, *ApJ*, 434, 446  
 Kuraszkiewicz, J.K. et al., 2003, *ApJ*, 590, 128  
 Kushino, A., Ishisaki, Y., Morita, U., Yamasaki, N.Y., Ishida, M., Ohashi, T. & Ueda, Y., 2002, *PASJ*, 54, 327  
 Lacy, M. et al., 2004, *ApJS*, 154, 166  
 La Franca, F. et al., 2005, *ApJ*, 635, 864  
 Laor, A. & Draine, B.T., 1993, *ApJ*, 402, 441  
 Lawrence, A., 1991, *MNRAS*, 252, 586  
 Lumb, D.H., Warwick, R.S., Page, M. & De Luca, A., 2002, *A&A*, 389, 93  
 Lutz, D., Maiolino, R., Spoon, H.W.W. & Moorwood, A.F.M., 2004, *A&A*, 418, 465  
 Maiolino, R. & Rieke, G.H., 1995, *ApJ*, 454, 95  
 Maiolino, R., Marconi, A. & Oliva, E., 2001, *A&A*, 365, 37  
 Manners, J. C., et al., 2003, *MNRAS*, 343, 293  
 Markwardt, C.B., Tueller, J., Skinner, G.K., Gehrels, N., Barthelmy, S.D. & Mushotzky, R.F., 2005, *ApJ*, 633, L77  
 Martínez-Sansigre, A., Rawlings, S., Lacy, M., Fadda, D., Marleau, F.R., Simpson, C., Wilott, C.J. & Jarvis, M.J., 2005, *Nature*, 436, 666  
 Martínez-Sansigre, A., Rawlings, S., Lacy, M., Fadda, D., Jarvis, M.J., Marleau, F.R., Simpson, C. & Wilott, C.J., 2006, *MNRAS*, in press (astro-ph/0604382)  
 Matt, G. et al., 1997, *A&A*, 325, L13  
 Minezaki, T., Yoshii, Y., Kobayashi, Y., Enya, K., Suganuma, M., Tomita, H., Koshida, S., Yamauchi, M. & Aoki, T., 2006, *ApJ*, 643, L5  
 Moran, E.C., Filippenko, A.V. & Chornock, R., 2002, *ApJ*, 579, L71  
 Mushotzky, R.F., Cowie, L.L., Barger, A.J. & Arnaud, K.A., 2000, *Nature*, 404, 459  
 Nandra, K., 2006, *MNRAS*, 368, L62  
 Nenkova, M., Ivezić, Ž. & Elitzur, M., 2002, *ApJ*, 570, L9  
 Netzer, H., Mainieri, V., Rosati, P. & Trakhtenbrot, B., 2006, *A&A*, 453, 525  
 Neugebauer, G. & Matthews, K., 1999, *AJ*, 118, 35  
 Neugebauer, G., Oke, J.B., Becklin, E.E. & Matthews, K., 1979, *ApJ*, 230, 79  
 Neugebauer, G., Miley, G. K., Soifer, B. T., & Clegg, P. E. 1986, *ApJ*, 308, 815  
 Papovich, C. et al., 2006, *ApJ*, 640, 92  
 Piconcelli, E., Jimenez-Bailón, E., Guainazzi, M., Schartel, N., Rodríguez-Pascual, P.M. & Santos-Lleó, M., 2005, *A&A*, 432, 15  
 Pier, E.A. & Krolik, J.H., 1992, *ApJ*, 401, 99  
 Purcell, E.M., 1976, *ApJ*, 206, 685  
 Rieke, G.H., 1978, *ApJ*, 226, 550  
 Rieke, G.H. & Lebofsky, M.J., 1981, *ApJ*, 250, 87  
 Rigby, J.R. et al., 2004, *ApJS*, 154, 160  
 Rigby, J.R., Rieke, G.H., Donley, J.L., Alonso-Herrero, A. & Pérez-González, P.G., 2006, *ApJ*, 645, 115  
 Risaliti, G., Maiolino, R. & Salvati, M., 1999, *ApJ*, 522, 157

- Risaliti, G., Elvis, M. & Nicastro, F., 2002, *ApJ*, 571, 234  
Risaliti, G., Elvis, M., Fabbiano, G., Baldi, A. & Zezas, A., 2005, *ApJ*, 623, L93  
Sanders, D.B., Phinney, E.S., Neugebauer, G., Soifer, B.T. & Matthews, K., 1989, *ApJ*, 347, 29  
Schweitzer, M. et al., 2006, *ApJ*, in press (astro-ph/0606158)  
Sellgren, K., 1984, *ApJ*, 277, 623  
Shemmer, O. et al., 2006, *ApJ*, 644, 86  
Shi, Y., Rieke, G.H., Hines, D.C., Gorjian, V., Werner, M.W., Cleary, K., Low, F.J., Smith, P.S. & Bouwman, J., 2006, *ApJ*, submitted  
Silva, L., Maiolino, R. & Granato, G.L., 2004, *MNRAS*, 355, 973  
Simpson, C., 2005, *MNRAS*, 360, 565  
Spergel, D.N., et al., 2003, *ApJS*, 148, 175  
Spingolito, L. & Malkan, M.A., 1989, *ApJ*, 342, 83  
Steffen, A.T., Strateva, I., Brandt, W.N., Alexander, D.M., Koekemoer, A.M., Lehmer, B.D., Schneider, D.P. & Vignali, C., 2006, *AJ*, 131, 2826  
Stern, D., et al., 2005, *ApJ*, 631, 163  
Sturm, E., Hasinger, G., Lehmann, I., Mainieri, V., Genzel, R., Lehnert, M.D., Lutz, D. & Tacconi, L.J., 2006, *ApJ*, 642, 81  
Suganuma, M., Yoshii, Y., Kobayashi, Y., Minezaki, T., Enya, K., Tomita, H., Aoki, T., Koshida, S. & Peterson, B.A., 2006, *ApJ*, 639, 46  
Treister, E. & Urry, C.M., 2005, *ApJ*, 630, 115  
Treister, E. et al., 2004, *ApJ*, 616, 123  
Treister, E., Urry, C.M., Van Dуйne, J., Dickinson, M., Chary, R.-R., Alexander, D.M., Bauer, F., Natarajan, P. & Lira, P., 2006, *ApJ*, 640, 603  
Tozzi, P. et al., 2001, *ApJ*, 562, 42  
Tozzi, P. et al., 2006, *A&A*, 451, 457  
Ueda, Y., Akiyama, M., Ohta, K. & Miyaji, T., 2003, *ApJ*, 598, 886  
Van Hoof, P.A.M., Weingartner, J.C., Martin, P.G., Volk, K. & Ferland, G.J., 2004, *MNRAS*, 350, 1330  
Weedman, D.W., Hao, L., Higdon, S.J.U., Devost, D., Wu, Y., Charmandaris, V., Brandl, B., Bass, E. & Houck, J.R., 2005, *ApJ*, 633, 706  
Weingartner, J.C. & Draine, B.T., 2001, *ApJS*, 134, 263  
Weingartner, J.C. & Murray, N., 2002, *ApJ*, 580, 88  
Worsley, M.A., Fabian, A.C., Bauer, F.E., Alexander, D.M., Hasinger, G., Mateos, S., Brunner, H., Brandt, W.N. & Schneider, D.P., 2005, *MNRAS*, 357, 1281  
Yaqoob, T. & Padmanabhan, U., 2004, *ApJ*, 604, 63  
Yun, M.S. & Carilli, C.L., 2002, *ApJ*, 568, 88  
Zheng, W. et al., 2004, *ApJS*, 155, 73

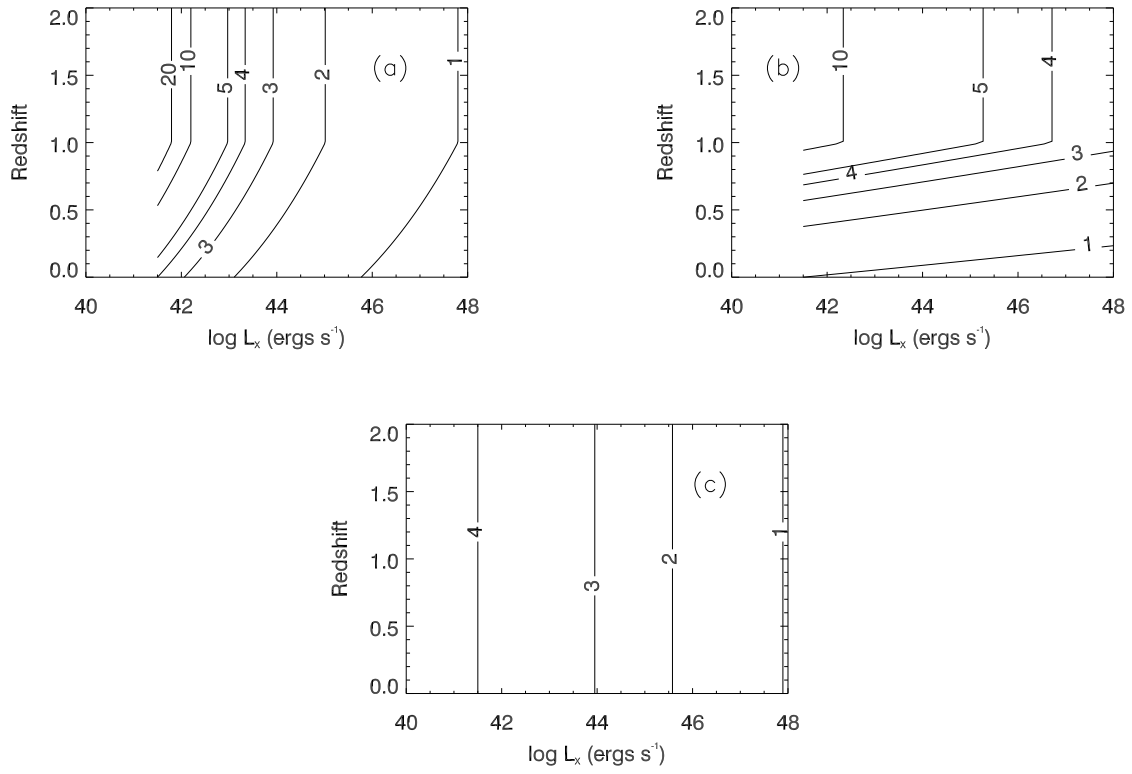


FIG. 1.— (a) Contours of the AGN type 2/type 1 ratio ( $R$ ) as a function of  $L_X$  and redshift for the evolution described by eqn. 3. Adapted from Ballantyne et al. (2006). Recall that the  $z$ -evolution is halted at  $z = 1$ . (b) Same as (a), but shows contours of  $R$  for the more rapid evolution of eqn. 4. (c) As in (a) and (b), but for a model with no redshift evolution (Eq. 5).

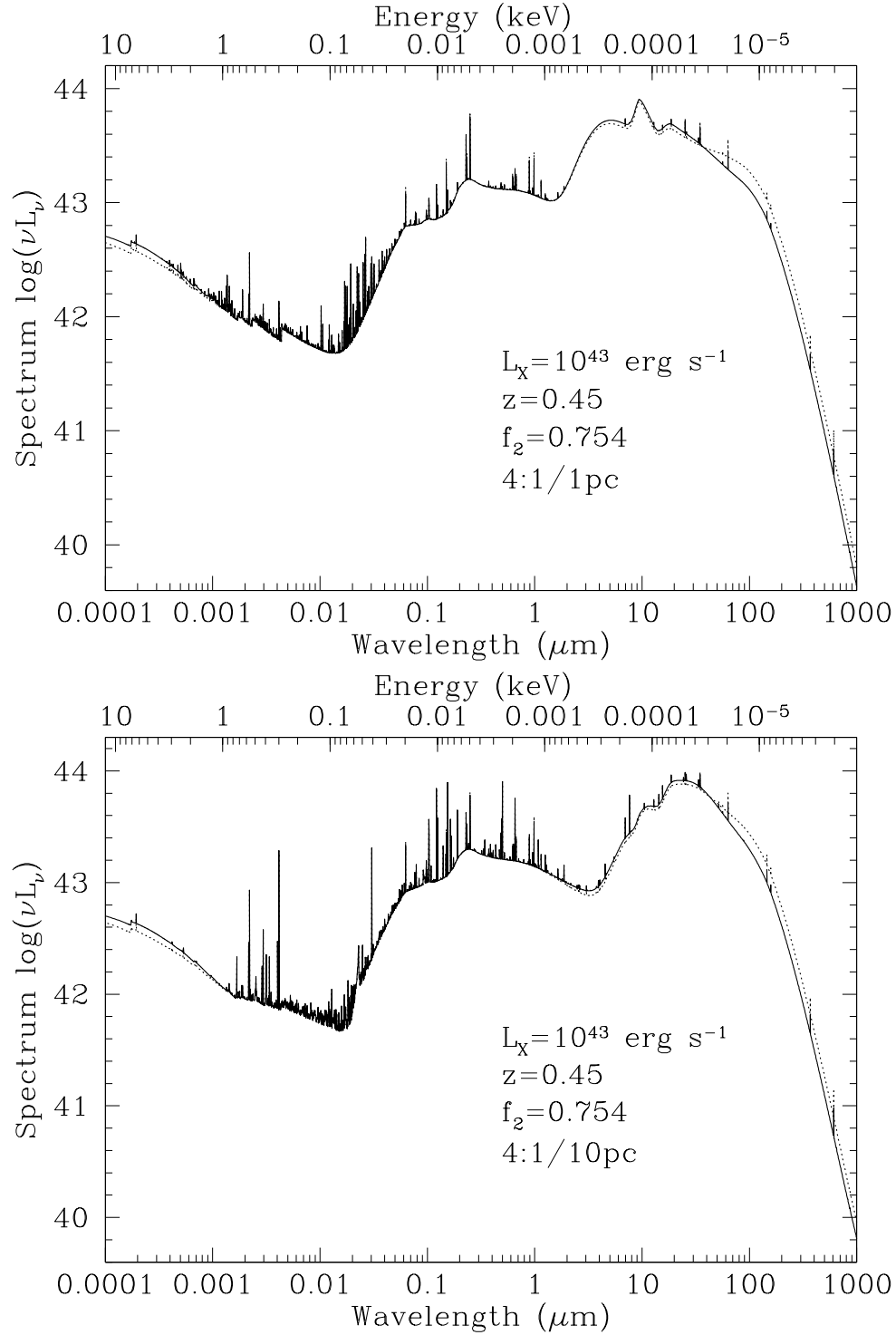


FIG. 2.— (Top) Example of a  $N_{\text{H}}$ -averaged SED. In this case, the illuminating AGN has a 2–10 keV luminosity of  $10^{43} \text{ erg s}^{-1}$ , and the inner radius of the absorbing gas is 1 pc from the ionizing source. This spectrum is taken from the 4:1 evolutionary grid (eqn. 3) when  $z = 0.45$ . Thus the fraction of type 2 AGN is  $f_2 = 0.754$ . The solid black line is the final  $N_{\text{H}}$ -averaged SED when the simple  $N_{\text{H}}$  distribution is assumed, while the dotted black line is the result when the Risaliti et al.  $N_{\text{H}}$  distribution is used. The Risaliti et al. distribution increases the emission longward of  $\sim 30 \mu\text{m}$ , and diminishes it between  $\sim 1$  and  $30 \mu\text{m}$ , as compared to the result with the uniform  $N_{\text{H}}$  distribution. (Bottom) As above, but with  $r = 10 \text{ pc}$ .



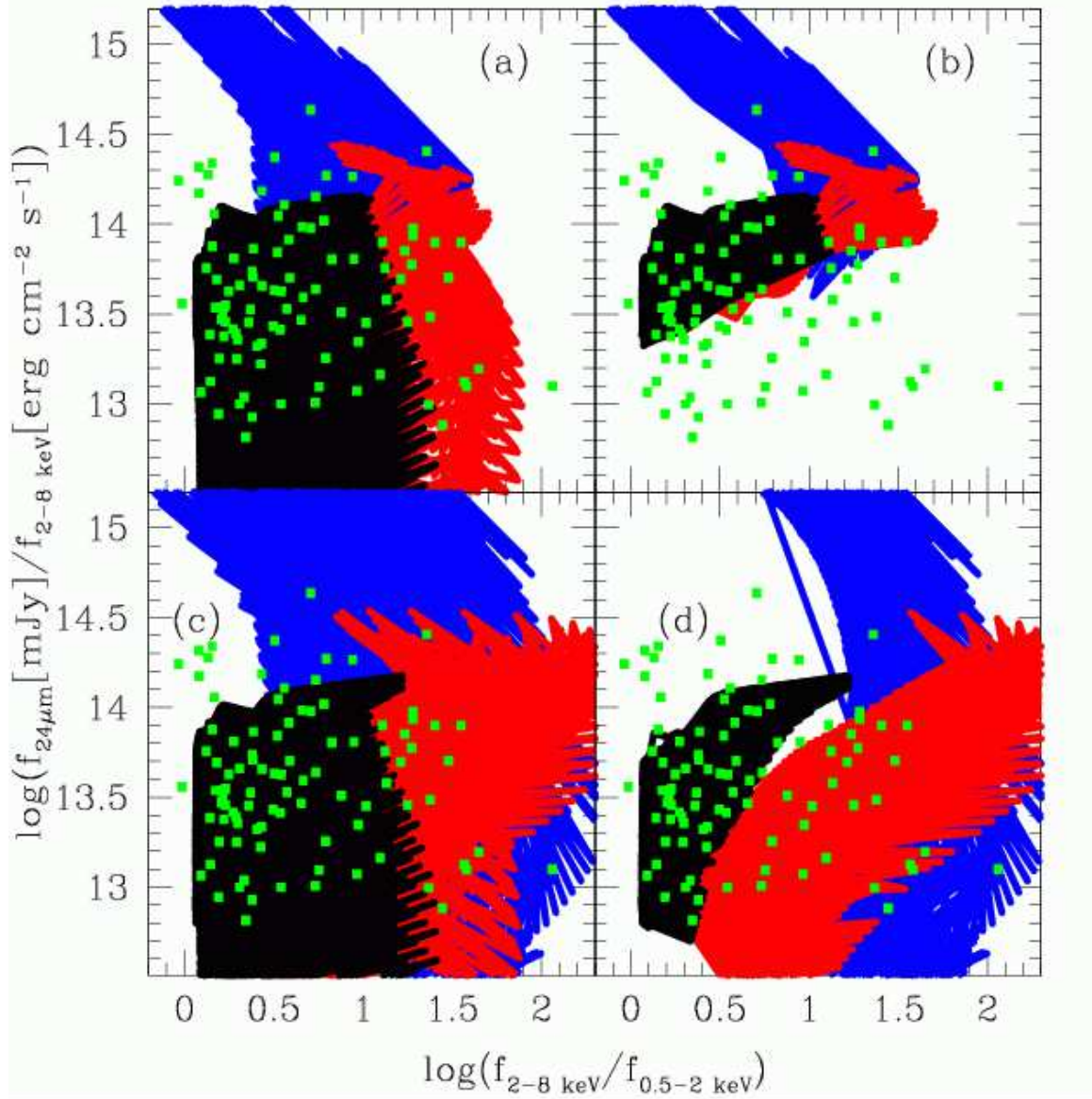


FIG. 3.— (a)  $24\mu\text{m}$  to 2–8 keV flux ratio versus X-ray hardness for all 4:1/1pc models with  $z < 3$  and  $\log L_X < 48$ . The fluxes are taken from the unified SEDs, i.e., before the final average over the  $N_{\text{H}}$  distribution. The blue region covers models with  $\log N_{\text{H}} \geq 24$ , the red area shows the results when  $23 \leq \log N_{\text{H}} < 24$ , and the black region is derived from models with  $\log N_{\text{H}} < 23$ . The green squares are data from the *Chandra* Deep Field South taken from Fig. 2 in the paper by Rigby et al. (2004). (b) As in (a) except only models with  $\log L_X < 43$  are plotted. (c) As in (a) except the results are taken from the 4:1/10pc grid. (d) As in (b) except the results are taken from the 4:1/10pc series of models.

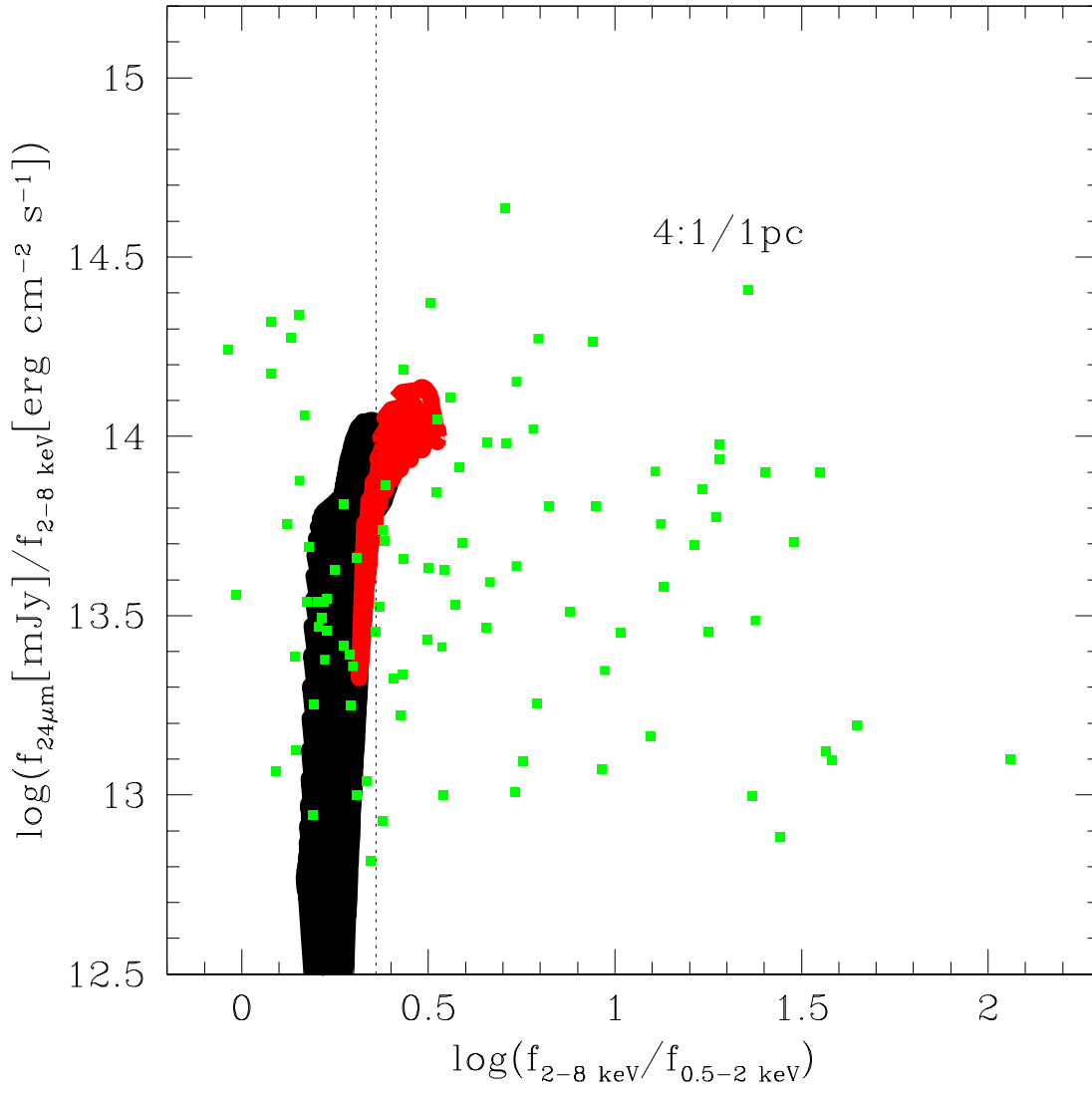


FIG. 4.— As in Figure 3(a) except the results for the final  $N_{\text{H}}$ -averaged SEDs are covered by the black region. As a result of the averaging, the final SEDs no longer span a large range of X-ray hardness. The red area corresponds to AGN with  $z < 1$  and  $\log L_X < 44$ . These sources produce the largest contribution to the CXRB and so must have a hardness ratio corresponding to a  $\Gamma = 1.4$  power-law (i.e.,  $\log(f_{2-8 \text{ keV}}/f_{0.5-2 \text{ keV}}) = 0.36$ , plotted as a dotted line). Sources at higher redshift will appear softer.

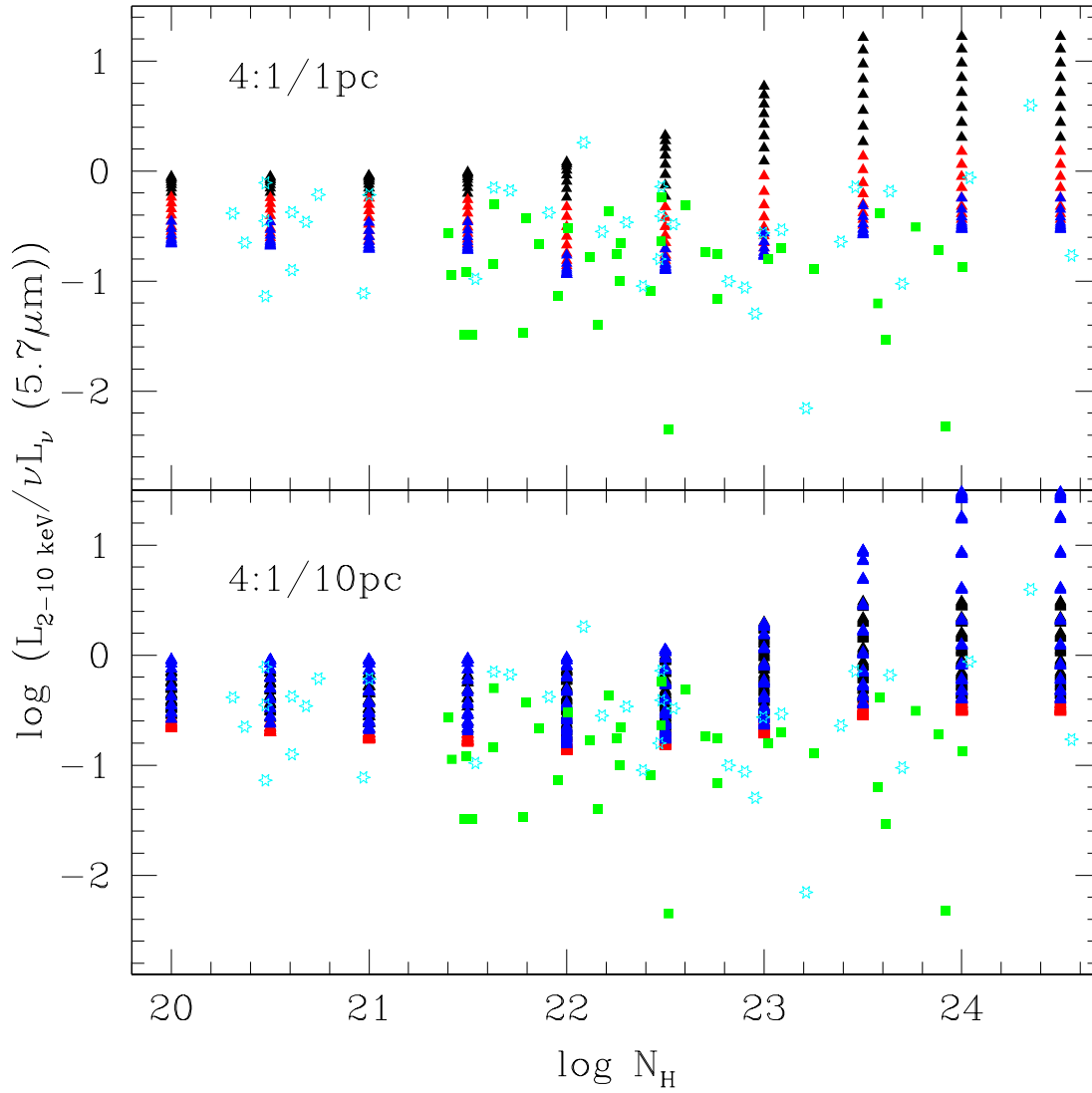


FIG. 5.— The ratio of input  $L_X$  to  $\nu L_\nu(5.7\mu\text{m})$  plotted versus  $\log N_H$  using the unified SEDs from the 4:1/1pc (top) and 4:1/10pc (bottom) grids. The points are color-coded by  $L_X$ : black triangles denote  $46 < \log L_X \leq 48$ , red triangles denote  $44 < \log L_X \leq 46$ , and blue triangles show results for  $41.5 \leq \log L_X \leq 44$ . Only models at  $z = 0.7$  are plotted, but as rest-frame luminosities are being plotted, there is little change at other redshifts. The green squares are data from both type 1 and 2 AGN taken from Rigby et al. (2006), while the cyan stars are data from Lutz et al. (2004). All of the observed data use  $6\mu\text{m}$  luminosities.

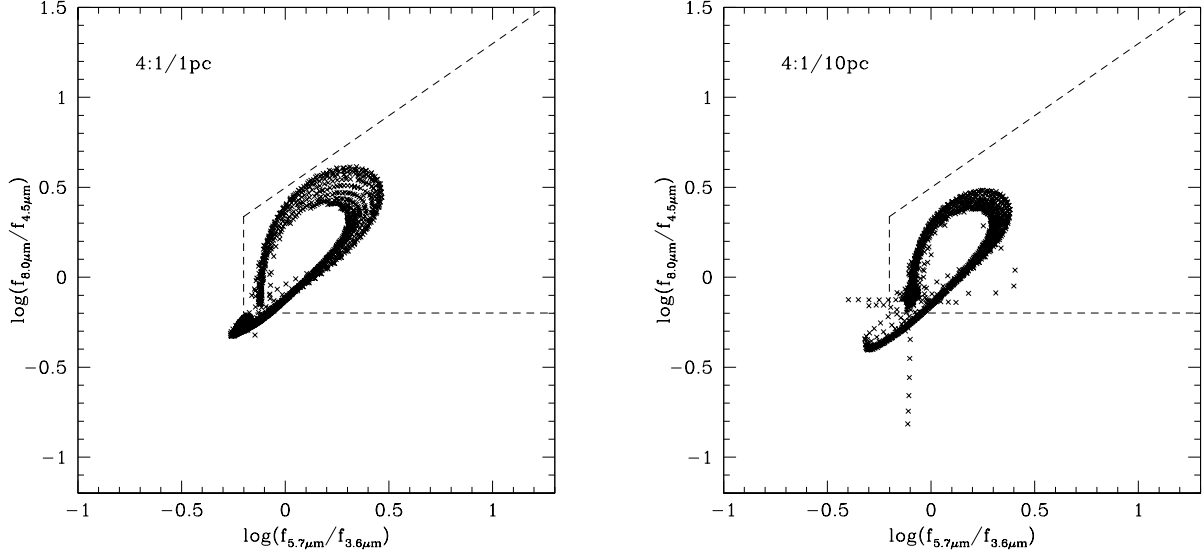


FIG. 6.— A color-color diagram for the 4 IRAC bands from *Spitzer*, after Lacy et al. (2004). (Left) The black crosses are the colors predicted from the 4:1/1pc  $N_{\text{H}}$ -averaged SEDs when  $z < 3$ . All  $L_X$  are included in this diagram. The region enclosed by the three dashed lines is the AGN selection region used by Lacy et al. (2004). (Right) Same as left-hand panel, but results are plotted for the 4:1/10pc grid.

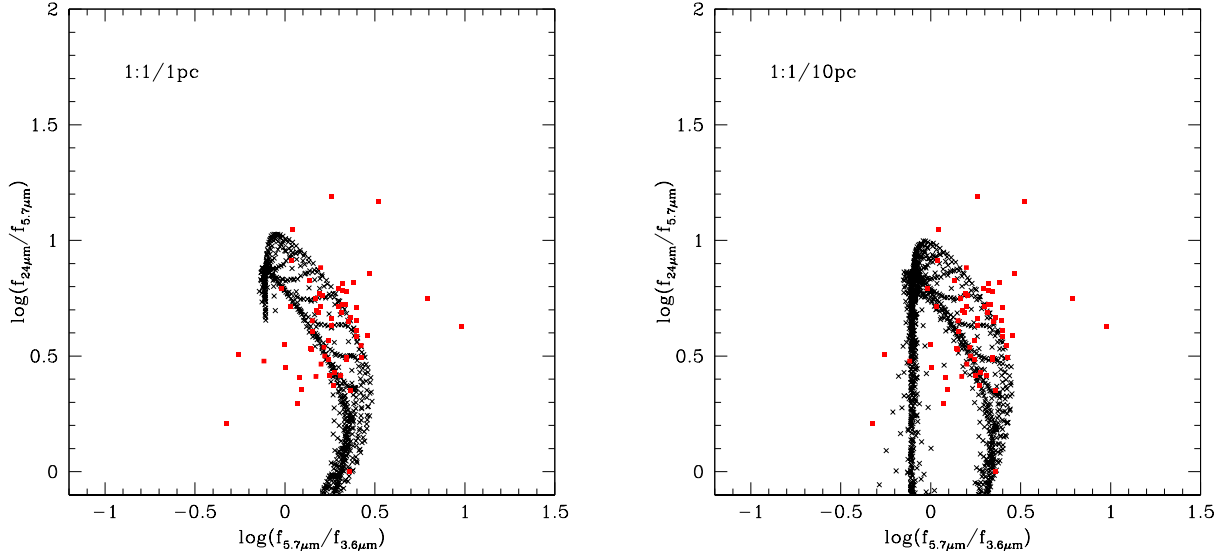


FIG. 7.— A color-color diagram across the MIPS-IRAC bands from *Spitzer*, after Lacy et al. (2004). (Left) The black crosses are the colors predicted from the 1:1/1pc  $N_{\text{H}}$ -averaged SEDs when  $z < 3$ . All values of  $L_X$  are included in the figure. The red squares are the observed colors of a variety of AGN plotted by Lacy et al. (2004) in his Figure 2. (Right) Same as left-hand panel, but results are plotted for 1:1/10pc grid.

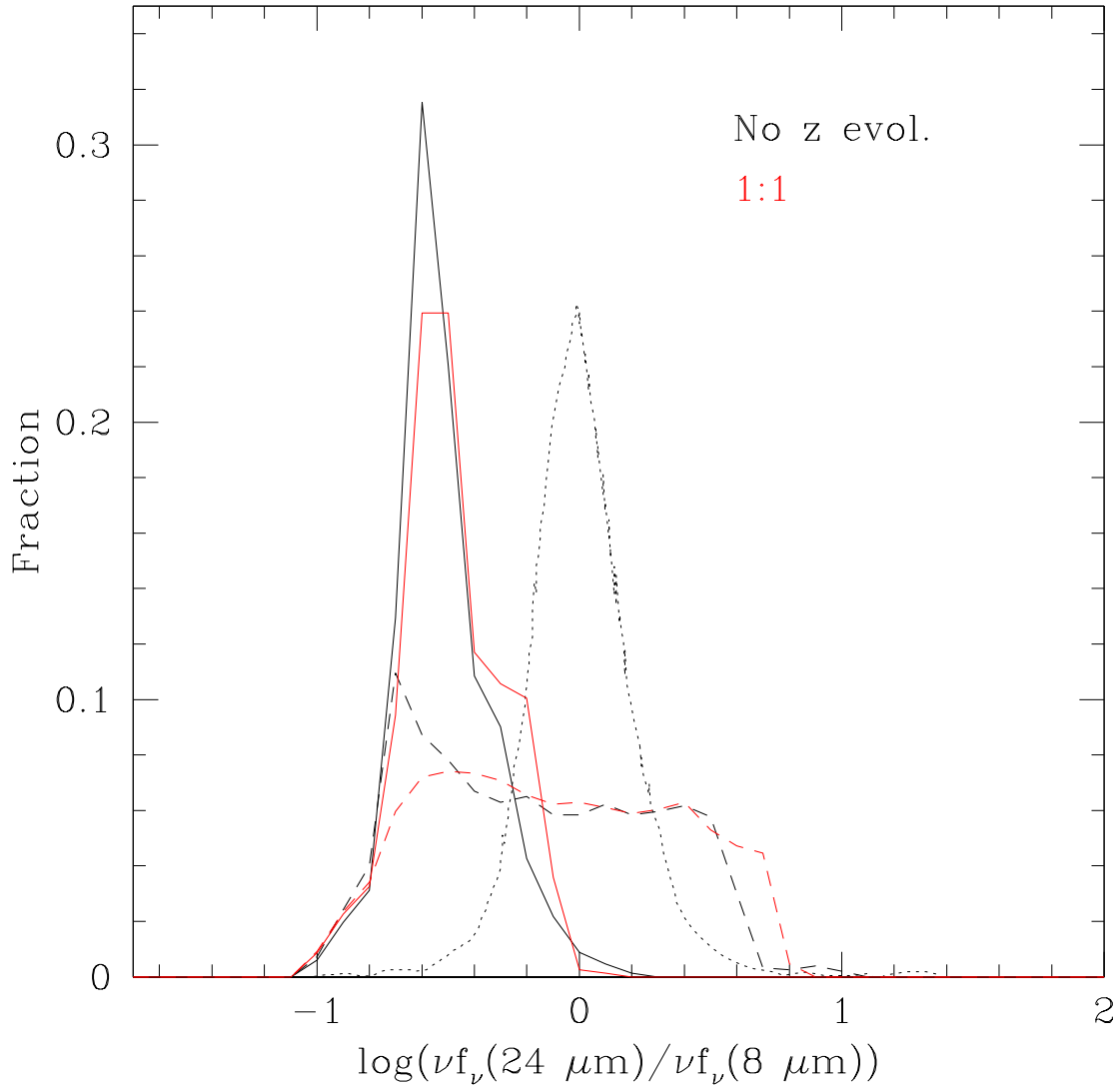


FIG. 8.— Histogram of the  $24\mu\text{m}/8\mu\text{m}$  flux ratio for sources in the nozevol/1pc (black solid line), the nozevol/10pc (black dashed line), the 1:1/1pc (red solid line) and the 1:1/10pc (red dashed line) grids. The dotted-line plots the histogram of flux ratios observed from X-ray selected AGN in the XBoötes survey (Brand et al. 2006). Only the models with  $f_{0.5-7 \text{ keV}} > 7.8 \times 10^{-15} \text{ erg cm}^{-2} \text{ s}^{-1}$ , the flux limit of the XBoötes survey, and  $f_\nu(24\mu\text{m}) > 0.3 \text{ mJy}$  are plotted in the figure.

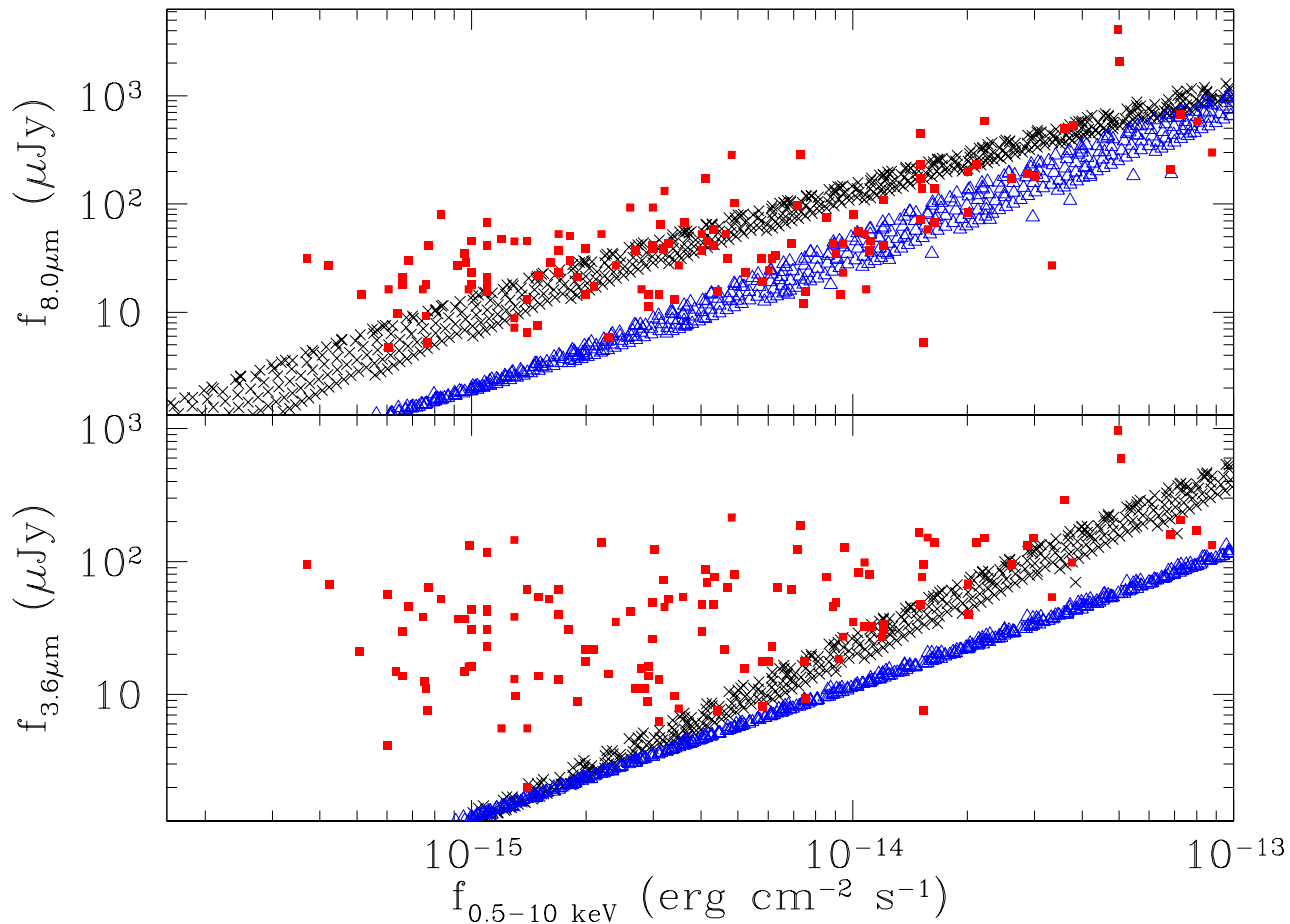


FIG. 9.— (Top) The predicted  $8\mu\text{m}$  flux is plotted against the  $0.5\text{--}10\text{ keV}$  X-ray flux. The black crosses denote results from the  $4:1/1\text{pc}$  grid, while the blue triangles are from the  $4:1/10\text{pc}$  grid. Predictions were only plotted for  $z < 3$ . The red squares are the observed fluxes from X-ray sources in the Extended Groth Strip taken from Fig. 7 in the paper by Barmby et al. (2006). (Bottom) As above, except the  $3.6\mu\text{m}$  flux is plotted against the  $0.5\text{--}10\text{ keV}$  flux.

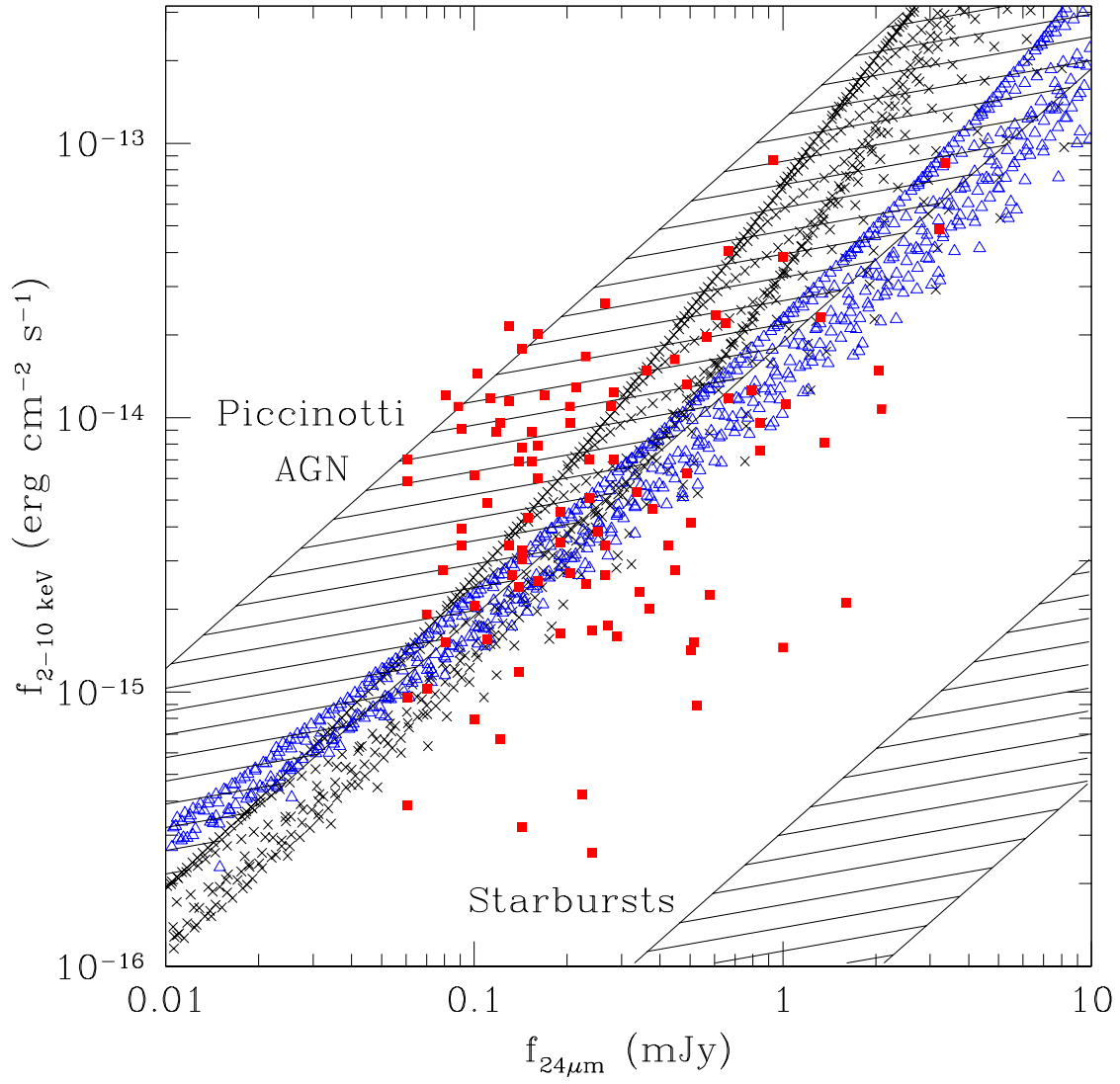


FIG. 10.— The predicted 2–10 keV flux is plotted against the  $24\mu\text{m}$  flux. The symbols are the same as Fig. 9, except the red squares are data from the *Chandra* Deep Field South taken from Fig. 1 in the paper by Alonso-Herrero et al. (2006). The hatched regions denote the extrapolation of the hard X-ray to mid-IR ratios for low-redshift X-ray selected AGN (‘Piccinotti AGN’) and local starburst galaxies (see Alonso-Herrero et al. 2004, 2006).

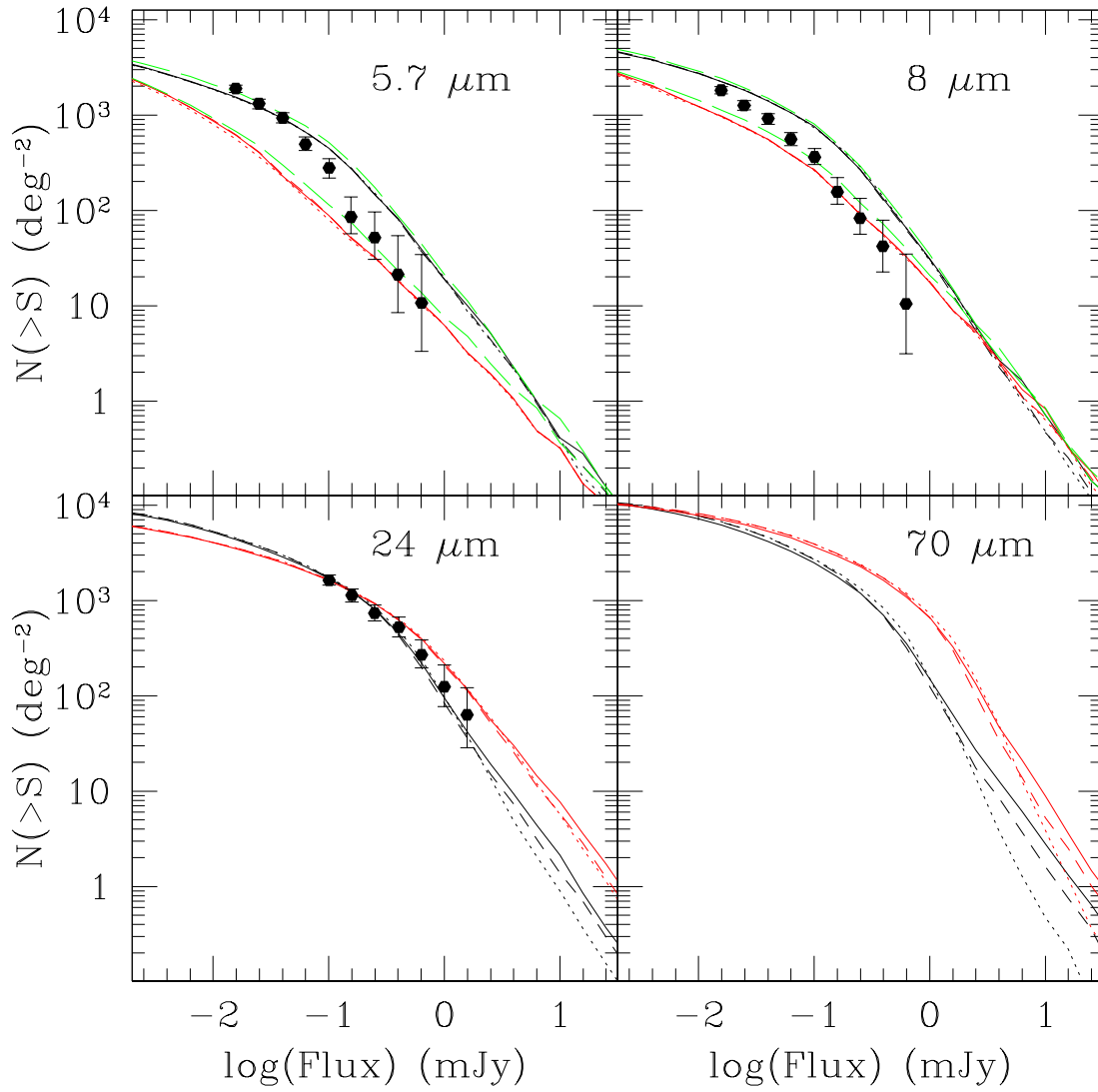


FIG. 11.— Cumulative number count distributions for 5.7, 8, 24 and 70 $\mu$ m. The black lines plot the predicted distributions from the models with the inner radius of the attenuating gas and dust at  $r = 1$  pc from the ionizing source, while the red lines show the results when  $r = 10$  pc. The solid lines denote the no  $z$  evolution model, while the dotted and dashed lines plot the 1:1 and 4:1 evolving models respectively. Green dashed lines show results for the non-evolving model computed with ISM grains. They are only relevant for the 5.7 and 8 $\mu$ m panels. The simple  $N_{\text{H}}$  distribution has been used in constructing the distributions. The data points in the 5.7, 8, and 24 $\mu$ m panels are taken from the GOODS survey of X-ray selected AGN (Treister et al. 2006).



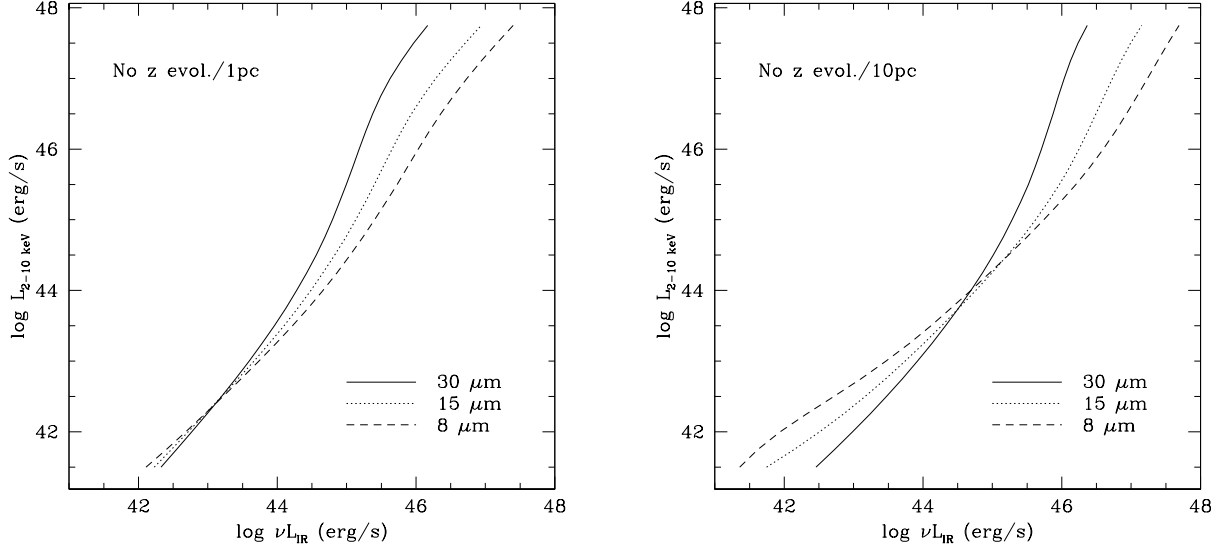


FIG. 12.— Input hard X-ray luminosity versus predicted IR luminosity for the  $N_{\text{H}}$ -averaged SEDs in the nozevol/1pc (left panel) and nozevol/10pc (right panel) grids. As indicated in the figures, the various line styles denote different IR wavelengths. The range of luminosity spanned in the infrared is smaller than the range in the X-ray, with the longer wavelengths covering smaller ranges.

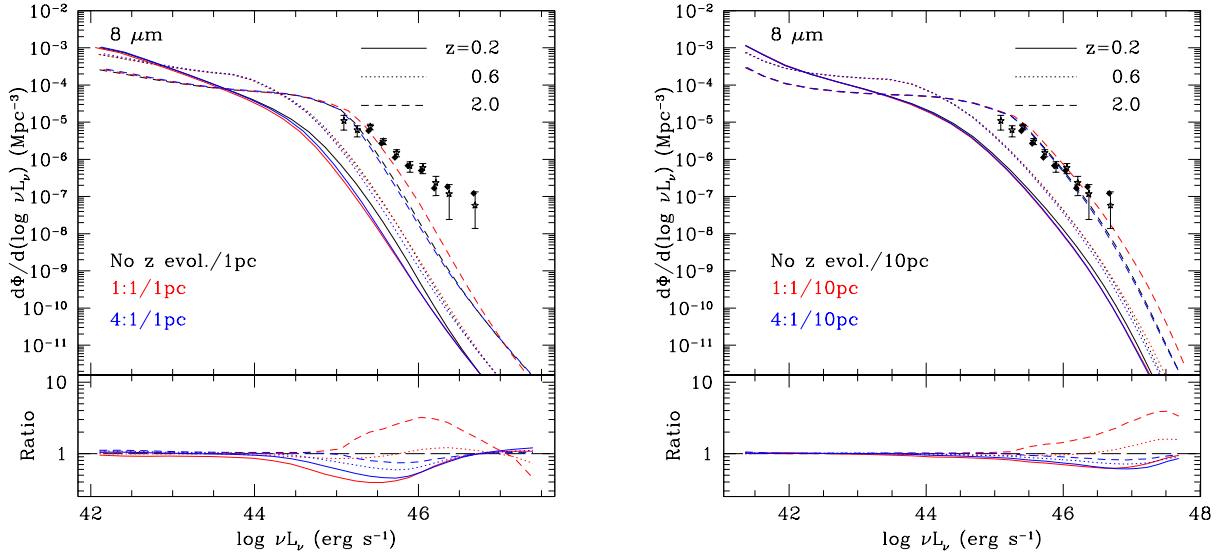


FIG. 13.— (Left) Predicted rest-frame AGN  $8\mu\text{m}$  luminosity functions for the three different evolutions of the type 2/type 1 ratio. The black lines show the results for the nozevol/1pc grid, the red lines denote the 1:1/1pc grid, and the blue lines plot the 4:1/1pc results. Three different redshifts are plotted using different line styles. The solid, dotted and dashed lines show the luminosity functions at  $z = 0.2, 0.6$  and  $2.0$ , respectively. The lower panel plots the ratio of the evolving luminosity functions to the non-evolving one for the three different redshifts. The colors denote the different evolving models as in the upper panel. For example, in the lower-panel the red-dashed line plots the ratio of the predicted 1:1/1pc luminosity function at  $z = 2$  to the predicted nozevol/1pc luminosity function at  $z = 2$ . The data points are the measured luminosity function of type 1 quasars determined by Brown et al. (2006), with the stars denoting objects with  $1 \leq z \leq 5$  and the diamonds are objects with  $1.5 \leq z \leq 2.5$ . (Right) As in the left-hand side, but for models with the inner radius of the absorbing gas and dust at a distance of 10 pc from the AGN.

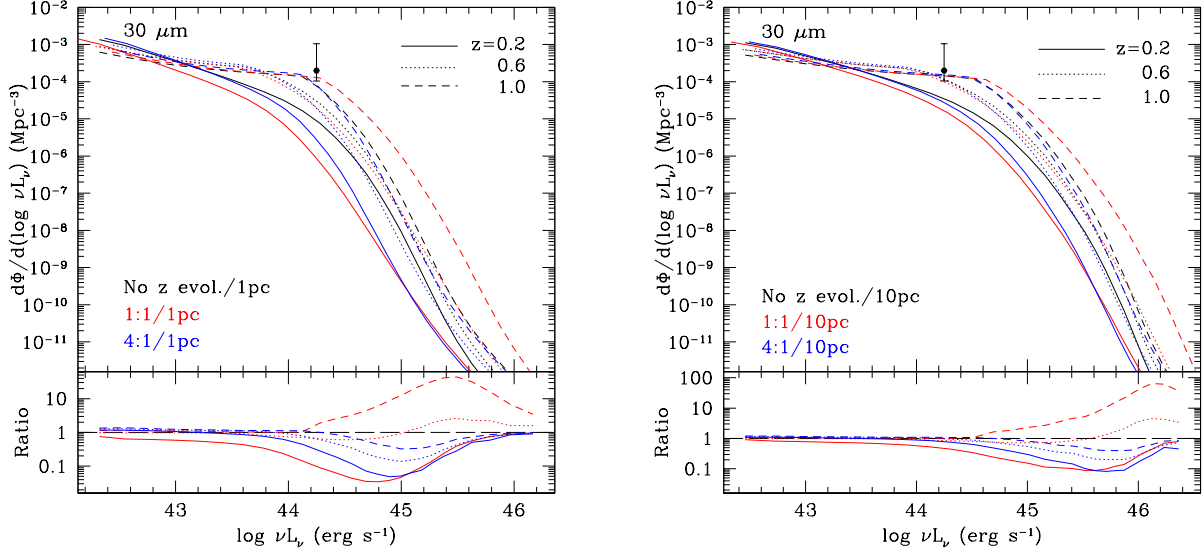


FIG. 14.— As in Fig. 13 except for the rest-frame  $30\mu\text{m}$  luminosity functions. The data point is calculated from the SWIRE survey of Franceschini et al. (2005). See text for details.

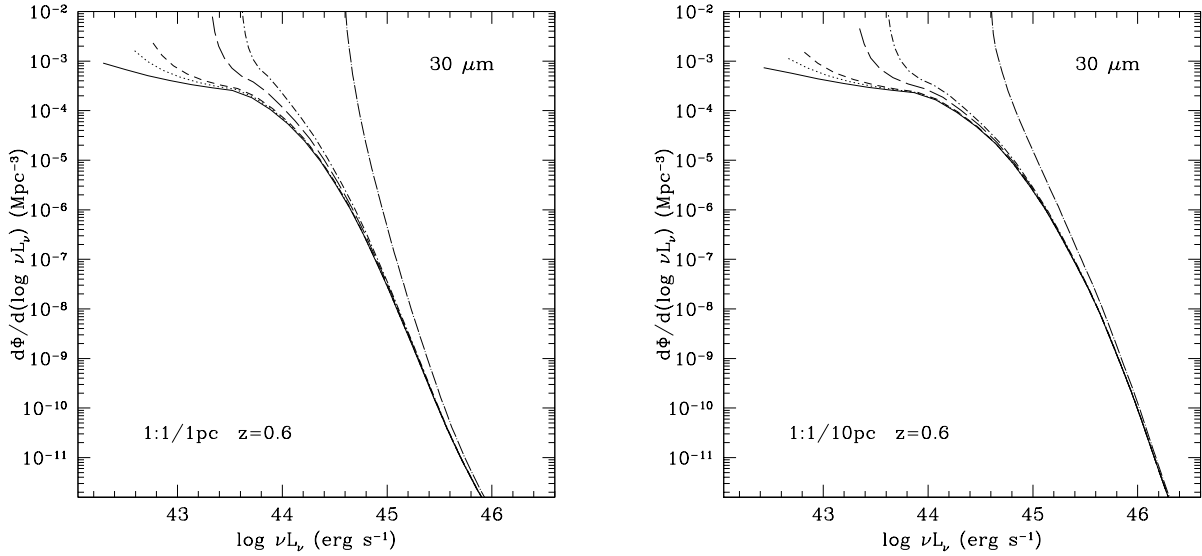


FIG. 15.— The predicted rest-frame  $30\mu\text{m}$  luminosity functions from the 1:1 grids at  $z = 0.6$ . The solid line has no contribution from star-formation and is identical to the equivalent curve in Fig. 14. The other line styles show the prediction when a constant SFR is included using the dust emission spectrum of eqn. 7: dotted-line= $0.5 M_{\odot} \text{ yr}^{-1}$ , short-dashed line= $1 M_{\odot} \text{ yr}^{-1}$ , long-dashed line= $5 M_{\odot} \text{ yr}^{-1}$ , short dot-dashed line= $10 M_{\odot} \text{ yr}^{-1}$ , long dot-dashed line= $100 M_{\odot} \text{ yr}^{-1}$ . The left(right)-hand panel contains the results when the inner radius of the attenuating material is at 1(10) pc from the AGN.

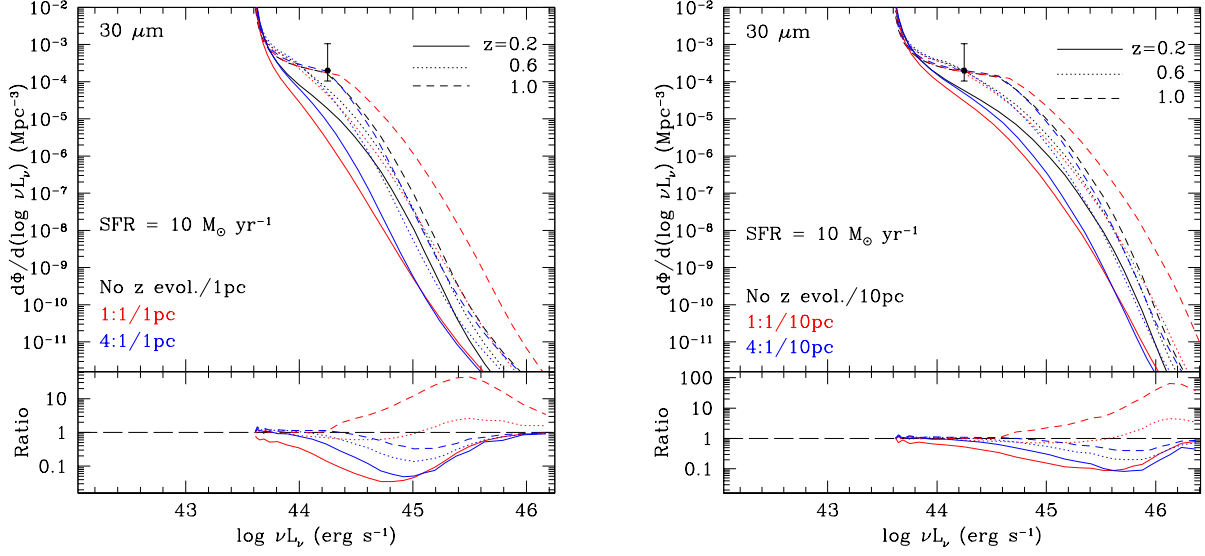


FIG. 16.— As in Fig. 14, but now including dust emission from a constant SFR of  $10 M_{\odot} \text{ yr}^{-1}$ .

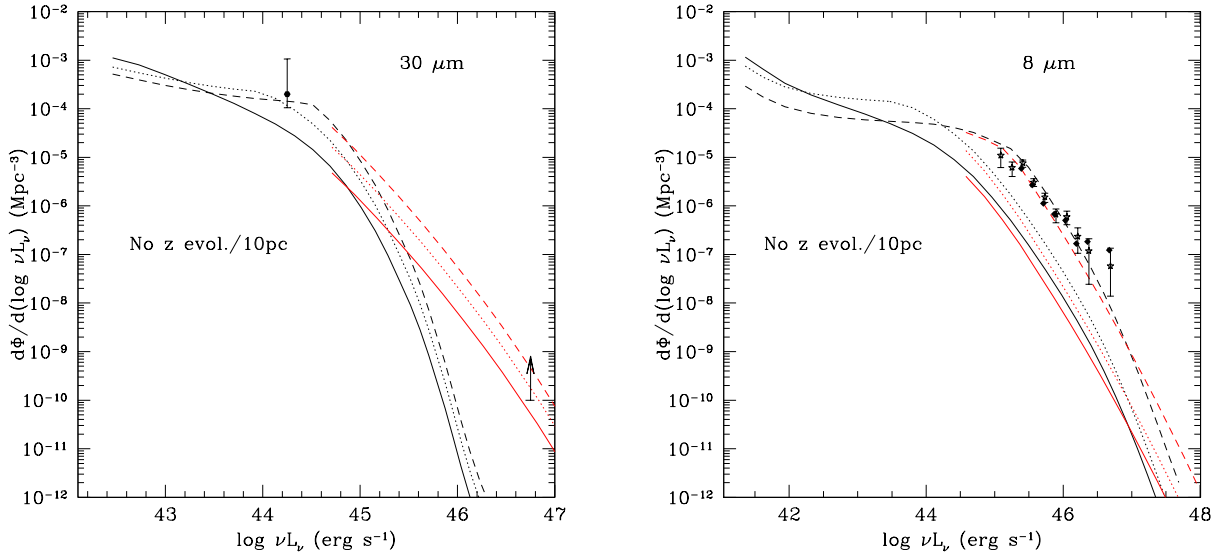


FIG. 17.— (Left) Plot of the rest-frame  $30\mu\text{m}$  LF at  $z = 0.2, 0.6$  and  $1.0$  (line styles and low-luminosity data point as in Fig. 14). The LFs were computed using the nozevol/10pc model grid. The arrow denotes the lower-limit to the high-luminosity rest-frame  $30\mu\text{m}$  LF at  $z = 1$  derived from *IRAS* sources (see text). The black lines are identical to the corresponding ones from Fig. 14 and plot the predictions using the assumed compact geometry described in Sect. 3.2. The red lines show the high- $\nu L_{\nu}$  results when the density of the absorbing cloud is lowered to  $100 \text{ cm}^{-3}$ . The absorber extends to much greater distances than the previous case, and therefore enhances the emission in the mid-IR. (Right) As in the left-hand plot, but for the rest-frame  $8\mu\text{m}$  LF. The line styles and points are the same as in Fig. 13.